Complex Conductivity of Graphitic Schists and Sandstones

F. Abdulsamad, A. Revil, A. Ghorbani, V. Toy, M. Kirilova, A. Coperey, P.A. A Duvillard, G. Ménard, Ludovic Ravanel

JGR Solid Earth

RESEARCH ARTICLE
10.1029/2019JB017628

Complex Conductivity of Graphitic Schists and Sandstones

F. Abdulsamad[1,2], A. Revil[1], A. Ghorbani[3], V. Toy[4], M. Kirilova[4], A. Coperey[1,2], P.A. Duvillard[1], G. Ménard[1], and L. Ravanel[1]

[1]EDYTEM, Université Grenoble Alpes, Université Savoie Mont-Blanc, CNRS, UMR CNRS 5204, Le Bourget du Lac, France, [2]Université Grenoble Alpes, Univ. Savoie Mont Blanc, CNRS, IRD, IFSTTAR, ISTerre, Grenoble, France, [3]Department of Mining and Metallurgical Engineering, Yazd University, Yazd, Iran, [4]Department of Geology, University of Otago, Dunedin, New Zealand

Key Points:
- Graphite-bearing rocks exhibit anomalous electrical properties
- New experimental data are shown to characterize the electrical properties of these rocks
- A model is developed to explain the new observations

Correspondence to:
A. Revil,
andre.revil@univ-smb.fr

Citation:
Abdulsamad, F., Revil, A., Ghorbani, A., Toy, V., Kirilova, M., Coperey, A., et al. (2019). Complex conductivity of graphitic schists and sandstones. *Journal of Geophysical Research: Solid Earth*, *124*, 8223–8249. https://doi.org/10.1029/2019JB017628

Received 3 MAR 2019
Accepted 31 JUL 2019
Accepted article online 7 AUG 2019
Published online 22 AUG 2019

Abstract Spectral induced polarization spectra were carried out on three graphitic schists and two graphitic sandstones. The microstructural arrangement of graphite of two graphitic schists was studied with thin sections using transmitted and reflected light optical and electron microscopic methods. Chemical maps of selected areas confirm the presence of carbon. The complex conductivity spectra were measured in the frequency range 10 mHz to 45 kHz and in the temperature range +20 °C down to −15 °C. The measured spectra are fitted with a double Cole-Cole complex conductivity model with one component associated with the polarization of graphite and the second component associated with the Maxwell-Wagner polarization. The Cole-Cole exponent and the chargeability are observed to be almost independent of temperature including in freezing conditions. The conductivity and relaxation time are dependent on the temperature in a predictable way. As long as the temperature decreases, the electrical conductivity decreases and the relaxation time increases. A finite element model is able to reproduce the observed results. In this model, we consider an intragrain polarization mechanism for the graphite and a change of the conductivity of the background material modeled with an exponential freezing curve. One of the core sample (a black schist), very rich in graphite, appears to be characterized by a very high conductivity (approximately 30 S/m). Two induced polarization profiles are discussed in the area of Thorens. The model is applied to the chargeability data to map the volumetric content of graphite.

1. Introduction

Induced polarization is a geophysical (galvanometric) method able to image the low-frequency polarization properties of rocks (e.g., Dahlin & Leroux, 2012; Schumberger, 1920). By "low frequency," we typically refer to frequencies below ~10 kHz. In this frequency range, the type of polarization mechanisms we are dealing with are nondielectric in nature. Induced polarization is indeed related to the accumulation or depletion of electrical charges at some characteristic length scales (typically grain/pore sizes) of the porous material and electro-diffusion mechanisms under the application of a primary electrical field (e.g., Marshall & Madden, 1959; Olhoeft, 1985). Induced polarization has a long history in mining geophysics as an efficient geophysical method to localize ores (e.g., Mahan et al., 1986; Schlumberger, 1920). That said, graphite-type rocks have not been thoroughly investigated in this context.

Schists are typically medium-grade metamorphic rocks with distinctly planar tectonite fabrics, that is, foliations (Passchier & Trouw, 2005). Schist foliations are defined by the presence of through going sheets of phyllosilicate minerals where individual grains are large enough to be seen by the naked eye. This mineral arrangement typically also imparts a tendency to break easily parallel to foliation planes (fissility). This arrangement is also responsible for an anisotropy of mechanical strength that is just one physical property affected by the foliation. It is reasonable to expect other physical properties of schists to be similarly anisotropic. The planar phyllosilicates that most commonly define the fabrics of these rocks are micas, but graphite-rich schists are also common with some black schists very rich in graphite formed by the medium-grade metamorphism of sediments initially rich in organic matter (Landis, 1971).

Graphite is a mineral consisting of layers of graphene made of carbon atoms bonded together in a hexagonal two-dimensional structure. Temperature has to exceed 400 °C to form crystalline graphite and the level of crystallinity depends on the degree of metamorphosis (Simandl et al., 2015). Graphite is considered one of the top 30 critical minerals in 2017 by the European Union (European Commission, 2017) for its use in

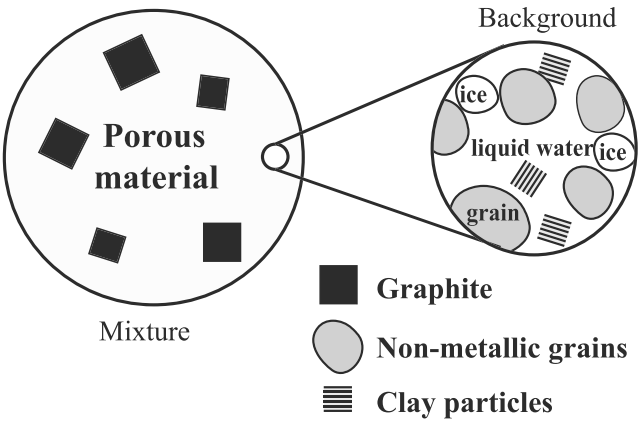

Figure 1. Sketch of the mixture between a background (made of nonmetallic grains and pore liquid water plus eventually some ice) and graphite. The background material can be partially saturated at a water content θ.

lubricants, electrodes, solar panels, and batteries. Since graphite is a semimetal, its electrical properties (like those of semiconductors and metals) have a strong influence on the conductivity and polarization properties of porous media in which they are located (Revil, Florsch, et al., 2015, Revil, Abdel Aal, et al., 2015; Revil, Coperey, Mao, et al., 2018). While it is broadly recognized that graphite is an excellent electrical conductor (e.g., Pierson, 1993), few works have addressed its polarization properties. The only work, to our knowledge, about the complex conductivity of graphitic schists is the recent paper by Börner et al. (2018). They measured the complex conductivity of a black schist and an augen gneiss both collected in the Main Central Thrust shear zone in the Himalayas of central Nepal. Their results underline the extraordinary high chargeability and anisotropy of the black schist with important consequences for interpreting magnetotelluric data in these environments. That said, this work remains very qualitative with respect to the body of fundamental knowledge accumulated over the last years in understanding the mechanisms of polarization of rocks with semiconductors, semimetals, and metals (Mao & Revil, 2016; Misra et al., 2016a, 2016b; Revil, Coperey, Mao, et al., 2018).

Our primary goal is in this paper is to develop a model of the complex conductivity of these rocks analyzing the effect of graphite on the complex conductivity of the whole rock (conduction and polarization). In order to test this model, we performed complex conductivity measurements on five core samples from the Alps (France and Switzerland). The spectra were obtained in the temperature +20 °C to −15 °C in order to better constrain the underlying physics of the conduction and polarization processes. We also performed an electrical conductivity experiment on pure graphite and polarization experiments at different volumetric contents of graphite in sand. In addition, we performed numerical experiments showing how the observed spectra can explain numerically the polarization process. In this case, we consider the electro-migration and charge accumulation in the graphite particles, themselves dispersed in a background material made of mineral (nonconducting) grains and pore water. Finally, we present induced polarization field data in which we image the conductivity and chargeability over two 600-m-long profiles carried out in Thorens (French Alps) in an area where permafrost and graphitic schists are known to be present.

2. Complex Conductivity of Rocks

2.1. A General Complex Conductivity Expression

In induced polarization, a rock is characterized in the frequency domain by its conductivity amplitude and its phase lag between the current and the electrical field. In this section, we consider an isotropic material made of metallic and nonmetallic grains and liquid pore water (Figure 1). The amplitude and phase can be recast into a complex-valued conductivity. The in-phase (real) component characterizes the ability of rocks to conduct an electrical current while its quadrature (out-of-phase, imaginary) conductivity describes the ability of rocks to reversibly store electrical charges (Olhoeft, 1981). Typically, the complex conductivity of a rock entering into Ampère's law is written as

$$\sigma^* = \sigma_\infty \left[1 - \frac{M}{(i\omega\tau)^c}\right], \tag{1}$$

where σ^* denotes the complex conductivity, ω is the angular frequency (rad/s), σ_∞ denotes the instantaneous (high-frequency) conductivity of the rock (in S/m), σ_0 denotes the DC (steady state, direct current) conductivity (S/m), $M = (\sigma_\infty - \sigma_0)/\sigma_\infty$ (dimensionless) denotes its chargeability, τ (in s) is the Cole-Cole relaxation time, and c (dimensionless) denotes the Cole-Cole exponent measuring the broadness of the distribution of the relaxation times (Cole & Cole, 1941).

A generalization of this equation for k-induced polarization distributions plus an explicit relationship for the Maxwell Wagner polarization can be written as

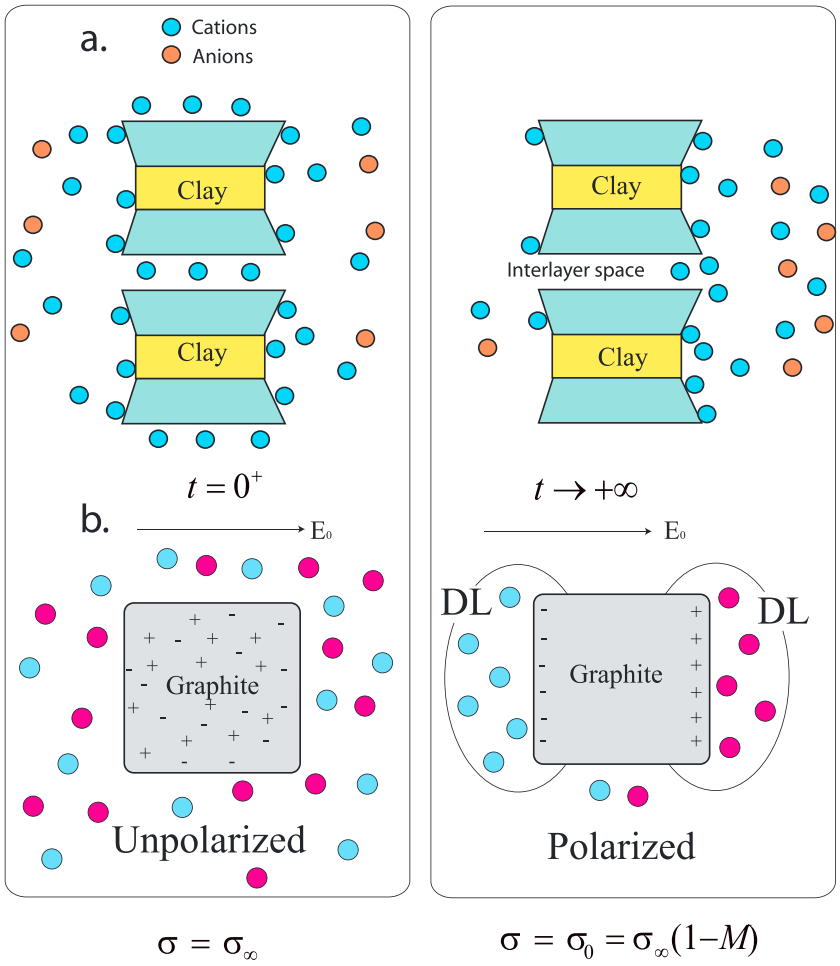

Figure 2. Sketch of the polarization of the nonmetallic grains and graphite. (a) The nonmetallic grain such as clays possesses an electrical double layer. Under the influence of an external electrical field $\mathbf{E}_0$, this electrical double layer polarizes. (b) Polarization of graphite. The charges carriers inside the grain (delocalized electrons and p-holes) polarize the grain giving then rise to the formation of field-induced diffuse layers (DL). The first column defined the instantaneous conductivity σ_∞ (where all charges carriers participate in the conduction process) while the second column defines the DC conductivity σ_0 (part of charges are no more available for conduction that is why $\sigma_\infty > \sigma_0$).

$$\sigma^* = \sigma_\infty\left(1-\sum_{k=1}^{K}\frac{M_k}{1+(i\omega\tau_k)^{c_k}}\right), \tag{2}$$

$$M_k = \frac{\sigma_k^\infty-\sigma_k^0}{\sigma_k^\infty}, \tag{3}$$

$$\sigma_0 = \sigma_\infty\left(1-\sum_{k=1}^{K}M_k\right), \tag{4}$$

where M_k, c_k, and τ_k denote the chargeability, the Cole-Cole exponent, and the relaxation time for process k for a total number of K polarization processes. For the two polarization processes, we have

$$\sigma^* = \sigma_\infty\left(1-\frac{M_1}{1+(i\omega\tau_1)^{c_1}}-\frac{M_2}{1+(i\omega\tau_2)^{c_2}}\right), \tag{5}$$

$$\sigma_\infty = \sigma_1^\infty + \sigma_2^\infty, \tag{6}$$

$$\sigma_0 = \sigma_\infty(1-M_1-M_2), \tag{7}$$

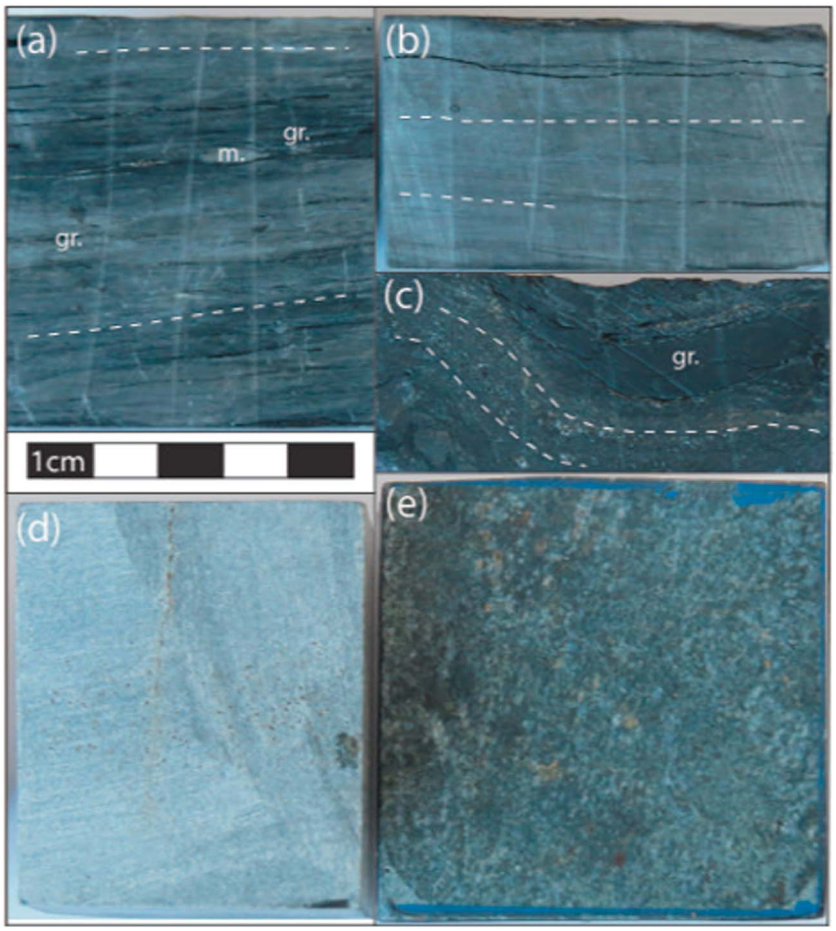

Figure 3. Pictures of cut faces of the five core samples. (a) Valt1 core sample (graphitic schist). (b) Valt2 core sample (graphitic schist). (c) ValT3 core sample (carbonized black schist). (d) S1 (graphitic tight sandstone 1). (e) S2 (graphitic tight sandstone 2). All the core samples are from Val Thorens (France) except core sample S2, which is from Mont-Fort (Swiss Alps, Switzerland). In (a)–(c) the traces of the schist foliations are highlighted by white dashed lines, and mica (m.) and graphite (gr.) pods are annotated.

where M_1 and M_2 are the chargeabilities (dimensionless), c_1 and c_2 are the two Cole-Cole exponents (dimensionless), and τ_1 and τ_2 are the relaxation times (expressed in s). The index 1 and 2 refer to two dispersion processes, respectively. With these relationships, we have

$$\sigma_0 \neq \sigma_1^0 + \sigma_2^0, \tag{8}$$

and $\sigma_1^\infty \neq \sigma_2^0$. If the total chargeability is defined by $M = (\sigma_\infty - \sigma_0)/\sigma_\infty$, we have $M_1 + M_2 = M$ from equation (7)

Table 1
Petrophysical Parameters of the Core Samples

Sample	Type	Origin	CEC (meq/100 g)	Porosity ϕ (-)	σ' (S/m) at 1 Hz (20 °C)	φ_m (-)
ValT1a	Graphitic schist (zone 1)	French Alps (Val Thorens)	2.1	0.042	0.00037	0.117
ValT1b	Graphitic schist (zone 1)	French Alps (Val Thorens)	2.1	0.042	0.015	0.117
ValT2a	Graphitic schist (zone 1)	French Alps (Val Thorens)	2.4	0.016	0.000687	0.089
ValT2b	Graphitic schist (zone 1)	French Alps (Val Thorens)	2.4	0.016	0.00171	0.089
ValT3	Schist carbonized	French Alps (Val Thorens)	5.6	0.147	39.64	Unknown
S1	Graphitic tight sandstone	French Alps (Val Thorens)	1.2	0.02	0.000151	0.054
S2	Graphitic tight sandstone	Switzerland Alps (Mont-Fort)	0.9	0.026	0.000505	0.031

Note. S1 and S2 correspond to two tight sandstones. Samples ValT1, ValT2, and ValT3 correspond to three graphitic schists. The volume fraction of graphite is determined from equation (18), which is validated by the data set shown in Figure 6c. The in-phase conductivity is reported at a pore water conductivity of 0.019 S/m (25 °C).

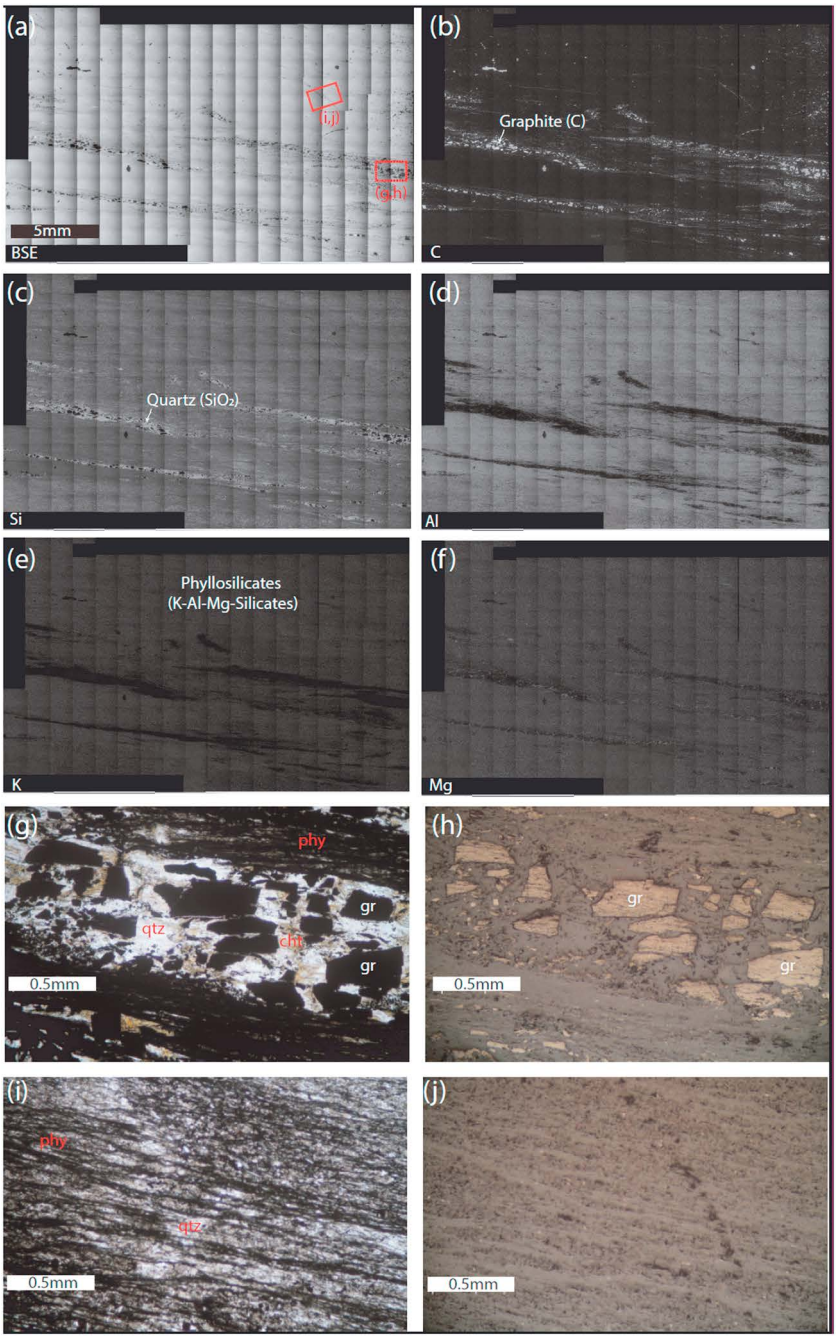

Figure 4. Sample ValT1. (a) Backscattered electron (BSE) image and (b–f) element maps acquired by electron dispersive spectroscopy (EDS) on a Zeiss Sigma SEM, operating at 8.5-mm WD, 15-keV accelerating voltage. Mapped element is labeled at bottom left of each image, and mineral phases consistent with the mapped mineralogy are also labeled. Photomicrographs in (g and i) plane-polarized light (PPL) and (h and j) reflected light highlight the two microstructures that dominate in these samples. (g and h) Mode 1: variable thickness and sometimes microfolded layers comprising large euhedral graphite (gr) grains surrounded by quartz (qtz) and chlorite (cht) pressure fringes. (i and j) Mode 2: disseminated graphite plus phyllosilicates (phy) with a weak foliation.

and since $0 \leq M \leq 1$, we have $0 \leq M_1+M_2 \leq 1$. In our model, one of the two mechanisms of polarization (for instance 1) would correspond to the polarization of graphite while the second mechanism (therefore mechanism 2) would correspond to the polarization of the electrical double layer of the insulating grains

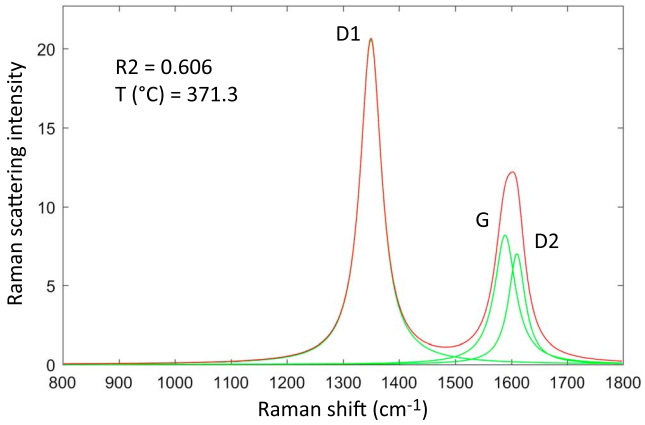

Figure 5. Representative Raman spectrum of graphite. D1, G, and D2 bands are fitted and illustrated. R_2 ratio and the estimated maximum metamorphic temperature (371 °C) are also provided.

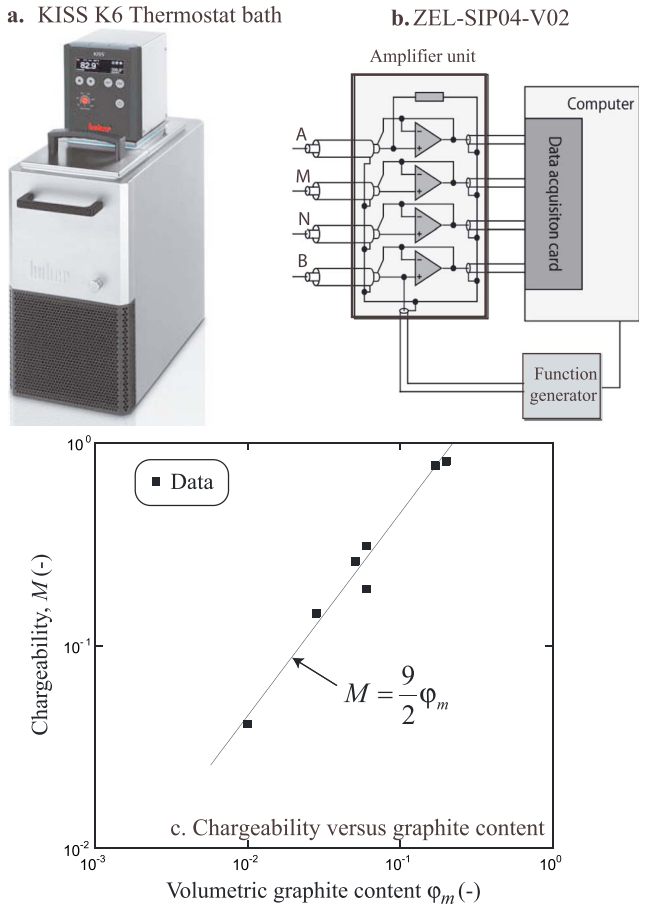

Figure 6. Equipment for the complex conductivity measurements. (a) Thermostat bath KISS K6 used for the temperature measurements. Dimensions 210 × 400 × 546 mm: bath volume 4.5 L. (b) Impedance meter ZEL-SIP04-V02 used for complex conductivity meter (see Zimmermann et al., 2008, for further details). (c) Chargeability versus graphite content for seven mixes of graphite and silica sand. The chargeability M was calculated from equation (3) by replacing the measured in-phase conductivity at the high and low frequency (10 kHz and 10 mHz). In this case, the sand used for the background had a very small chargeability (~10^{-3}).

forming the skeleton of the background material (Figure 2). A third polarization mechanism would correspond to the Maxwell-Wagner polarization (see Appendix A). The goal of the next subsections is to describe a model of polarization for these two components. In our experiments, we will focus however on this first contribution associated with graphite since a small amount of graphite (say 1% vol.) is enough to mask the background polarization.

2.2. The Contribution Associated With the Background

The instantaneous conductivity is the conductivity of the material just after the application of an electrical field (see Figure 2; high-frequency asymptotic conductivity in frequency domain induced polarization). The DC or stationary conductivity denotes a smaller conductivity including the effect of charge carrier blockage responsible for polarization (Figure 2). Using a volume-averaging approach, Revil (2013) obtained the following expressions for the high- and low-frequency conductivities of the background material (i.e., for the instantaneous conductivity and DC conductivity of the background material; see Figure 2),

$$\sigma_2^{\infty} = \frac{1}{F}\sigma_w + \left(\frac{1}{F\phi}\right)\rho_g B\mathrm{CEC}, \tag{9}$$

$$\sigma_2^{0} = \frac{1}{F}\sigma_w + \left(\frac{1}{F\phi}\right)\rho_g (B - \lambda)\mathrm{CEC}. \tag{10}$$

In these equations, σ_w (in S/m) denotes the pore water conductivity (which depends on both salinity and temperature), F (dimensionless) the intrinsic formation factor related to the connected porosity ϕ (dimensionless) by the first Archie's law $F = \phi^{-m}$ where m (dimensionless) is called the first Archie exponent or porosity exponent (Archie, 1942), ρ_g is the grain density (in kg/m^3, usually ρ_g = 2,650 kg/m^3), and the cation exchange capacity (CEC) denotes the cation exchange capacity (in C/kg and often expressed in meq/100 g with 1 meq/100 g = 963.20 °C/kg). The CEC is mainly sensitive to the clay type (e.g., kaolinite, illite, smectite) and the weight fraction of these clay minerals in the rock. In equations (9) and (10), the quantity B (expressed in m^2·s^{-1}·V^{-1}) denotes the apparent mobility of the counterions for surface conduction and the quantity λ (expressed in m^2·s^{-1}·V^{-1}) denotes the apparent mobility of the counterions for the polarization associated with the quadrature conductivity (see Revil et al., 2017, and references therein). A dimensionless number R is also introduced with

$$\mathrm{R} = \frac{\lambda}{B}, \tag{11}$$

(see Revil et al., 2017 for further explanations). This number is introduced because it corresponds to the maximum value of the chargeability in absence of metallic particles. From previous studies (e.g., Ghorbani et al., 2018), we have B (Na^+, 25 °C) = 3.1 ± 0.3 × 10^{-9} m^{-2}·s^{-1}·V^{-1} and λ (Na^+, 25 °C) = 3.0 ± 0.7 × 10^{-10} m^{-2}·s^{-1}·V^{-1}. These two quantities have been determined using large data sets of rock samples (including hundreds of core samples) and are therefore

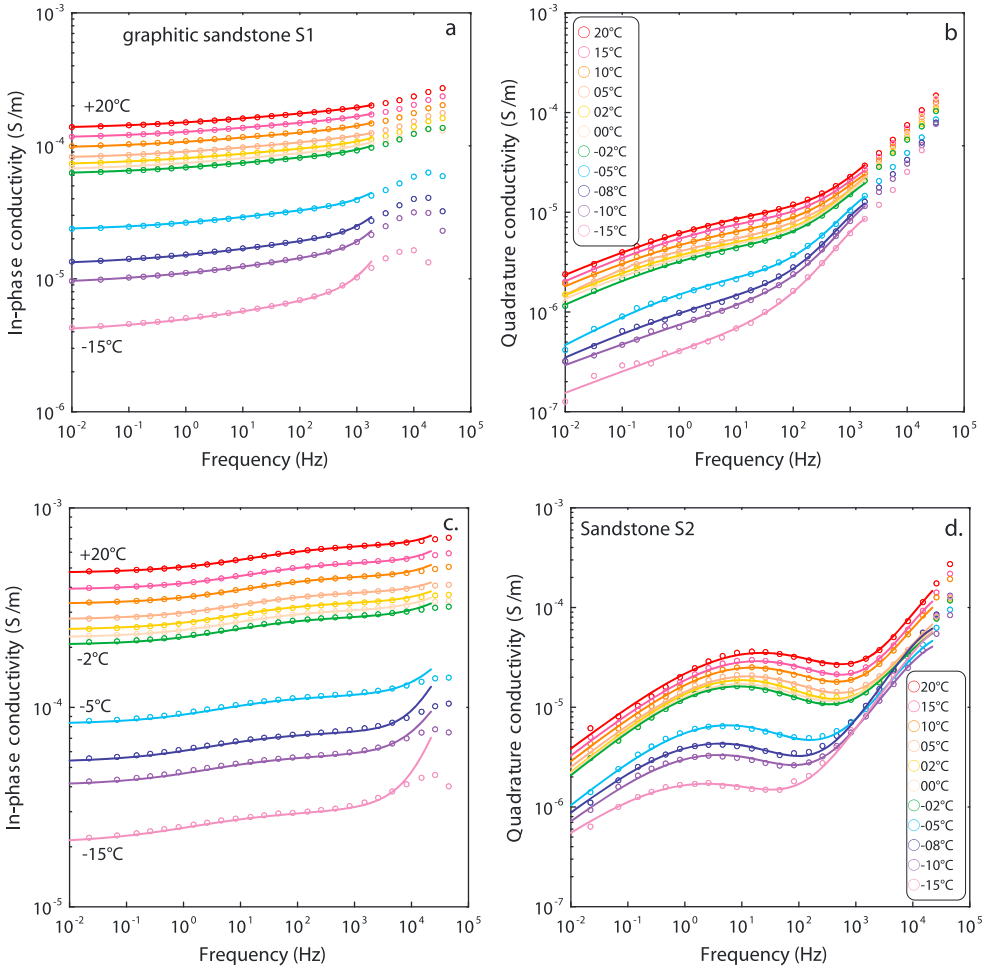

Figure 7. Complex conductivity spectra of samples S1 and S2. (a) In-phase conductivity of sample S1. (b) Quadrature conductivity of sample S1. (c) In-phase conductivity of sample S2 (the phase reaches ~100 mrad). (d) Quadrature conductivity of sample S2 (the phase reaches ~80 mrad at the peak frequency). The plain lines represent the fit of the data with a double Cole-Cole as described in Appendix A. The Cole-Cole parameters are reported in Tables 2–7. We did not try to fit the high frequencies because of electromagnetic effects and we did not try to interpret the Maxwell-Wagner polarization for the same reason. Only the data with an uncertainty smaller than 1% were considered in the Cole-Cole fit of the data.

reliable. It follows that the dimensionless number R is typically around 0.09 ± 0.01 (independent of the temperature and saturation; Revil, Coperey, Deng, et al., 2018).

From equations (3), (9), and (10), we obtain the following expression of the chargeability of the background,

$$M_2 = \frac{\rho_g \lambda \, \mathrm{CEC}}{\phi \sigma_w + \rho_g B \mathrm{CEC}}. \tag{12}$$

This equation shows explicitly the dependence between the background chargeability M_2, the pore water conductivity, and the CEC. We also have the property $M_2 \leq R \sim 0.09 \pm 0.01$. Therefore, the background chargeability is generally quite small (less than 10% or 100 mV/V).

The Cole-Cole time constant τ_2 is associated with a characteristic pore size Λ (in m; see Revil & Florsch, 2010; Revil et al., 2012) according to

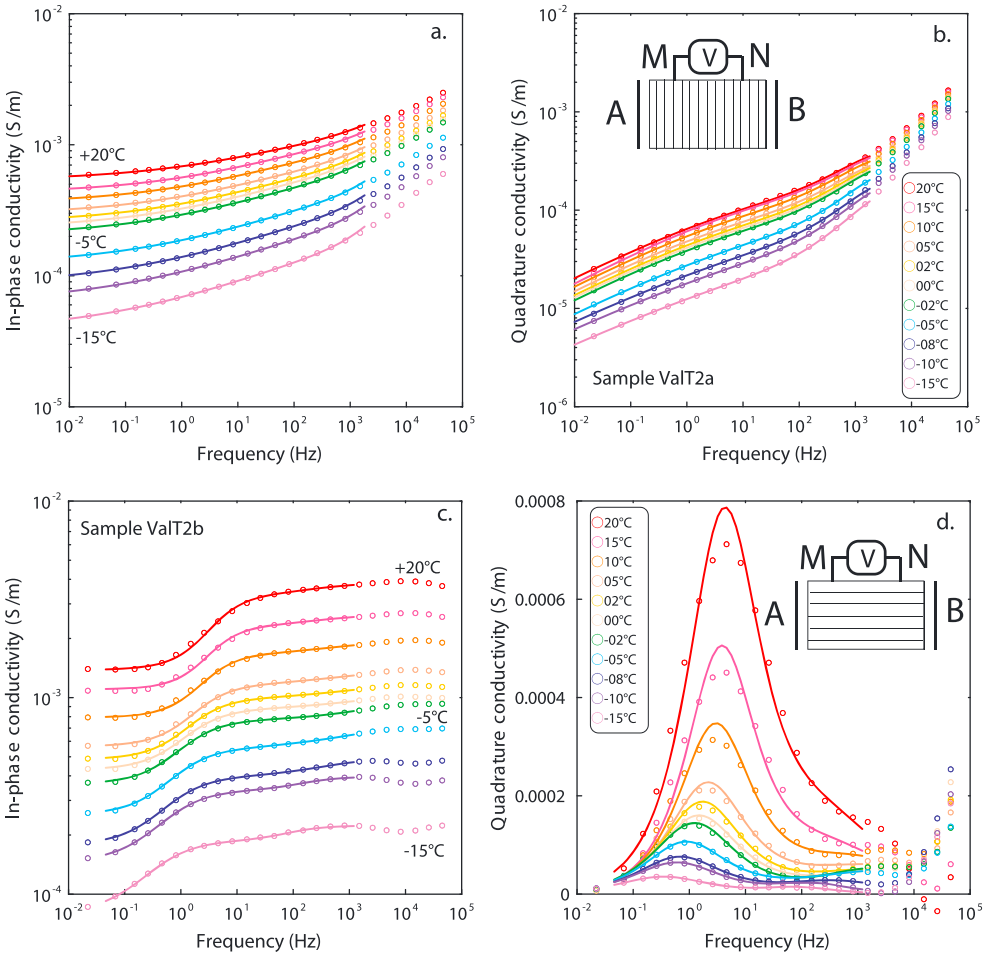

Figure 8. Complex conductivity spectra of sample ValT2. (a) In-phase conductivity (transverse component). (b) Quadrature conductivity (transverse component). The phase reaches ~200 mrad at its maximum. (c) In-phase conductivity (in-plane component). (d) Quadrature conductivity (in-plane component). The phase reaches ~300 mrad at the peak frequency. The plain lines represent the fit of the data with a double Cole-Cole as described in Appendix A. The Cole-Cole parameters are reported in Tables 2–7. The linear scale was used to better compare the data with the Cole-Cole fit. Only the data with an uncertainty smaller than 1% were considered in the Cole-Cole fit of the data.

$$\tau_2 = \frac{\Lambda^2}{2D^S_{(+)}}, \tag{13}$$

where $D^S_{(+)}$ denotes the diffusion coefficient of the counterions in the Stern layer (in m^2/s). The value of this diffusion coefficient $D^S_{(+)}$ should relate to the mobility of the counterions in the Stern layer, $\beta^S_{(+)}$, by the Nernst-Einstein relationship,

$$D^S_{(+)} = \frac{k_b T \beta^S_{(+)}}{\left|q_{(+)}\right|}, \tag{14}$$

where T denotes the absolute temperature (in K), k_b denotes the Boltzmann constant (1.3806×10^{-23} m^2 kg s^{-2} K^{-1}), and $|q_{(+)}|$ is the charge of the counterions in the Stern layer coating the surface of the grains ($|q_{(+)}| = e$ where e denotes the elementary charge for Na^+). Since each relaxation time depends on a pore size, the Cole-Cole exponent c_2 measures the broadness of the pore size distribution.

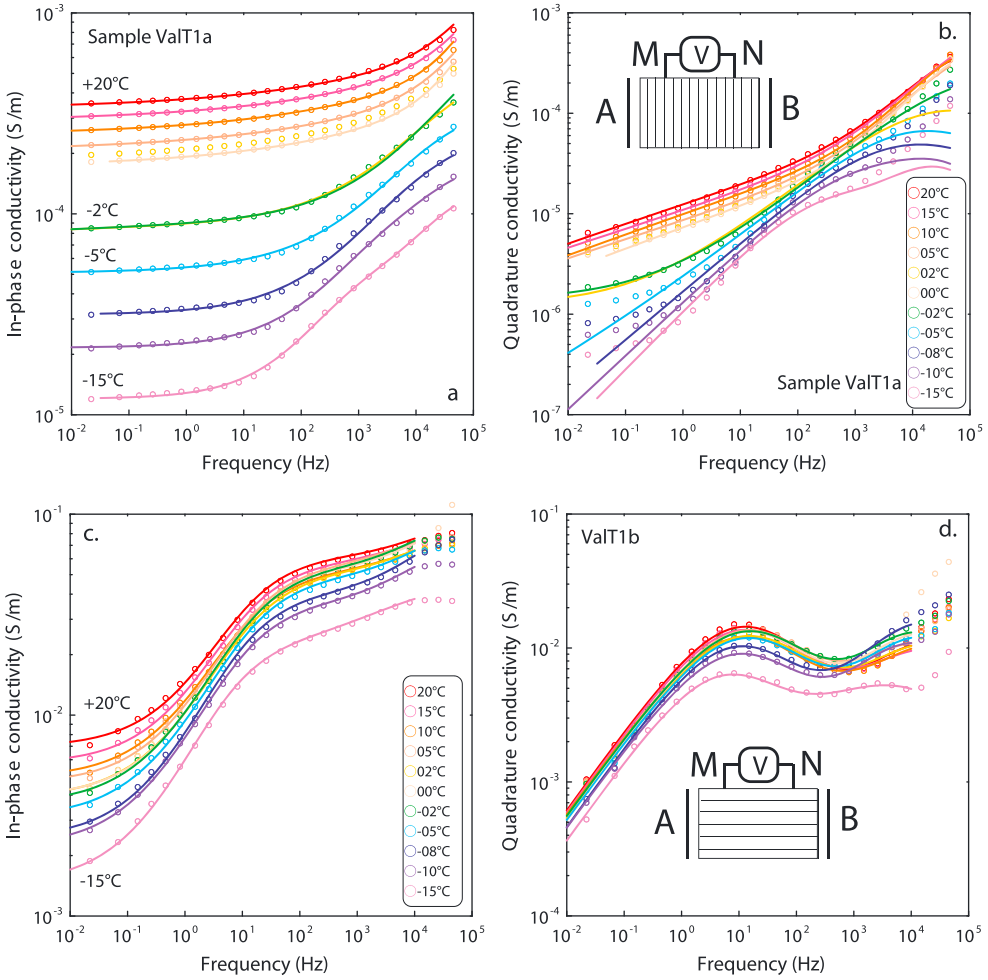

Figure 9. Complex conductivity spectra of sample ValT1. (a) In-phase conductivity (transverse component). (b) Quadrature conductivity (transverse component). The phase reaches ~400 mrad at its peak frequency. (c) In-phase conductivity (in-plane component). (d) Quadrature conductivity (in-plane component). The phase reaches ~600 mrad at the peak frequency. The plain lines represent the fit of the data with a double Cole-Cole as described in Appendix A. The Cole-Cole parameters are reported in Tables 2–7. Only the data with an uncertainty smaller than 1% were considered in the Cole-Cole fit of the data.

2.3. The Contribution Associated With Graphite

For a mixture of nonmetallic grains, pore water, and metallic grains, Revil, Florsch, et al., (2015), Revil, Abdel Aal, et al., (2015) have demonstrated that the chargeability of the mixture is given by

$$M = \frac{9}{2}\varphi_m + M_2, \tag{15}$$

where φ_m denote the volume fraction of metallic particles in the medium. In addition, the instantaneous and the steady state conductivities of the mixture are related to the instantaneous and steady state conductivities of the background material according to (Revil, Florsch, et al., 2015)

$$\sigma_\infty = \sigma_2^\infty(1 + 3\varphi_m + ...), \tag{16}$$

$$\sigma_0 = \sigma_2^0\left(1 - \frac{3}{2}\varphi_m + ...\right). \tag{17}$$

Using equations (5), (6), and (8), this implies that

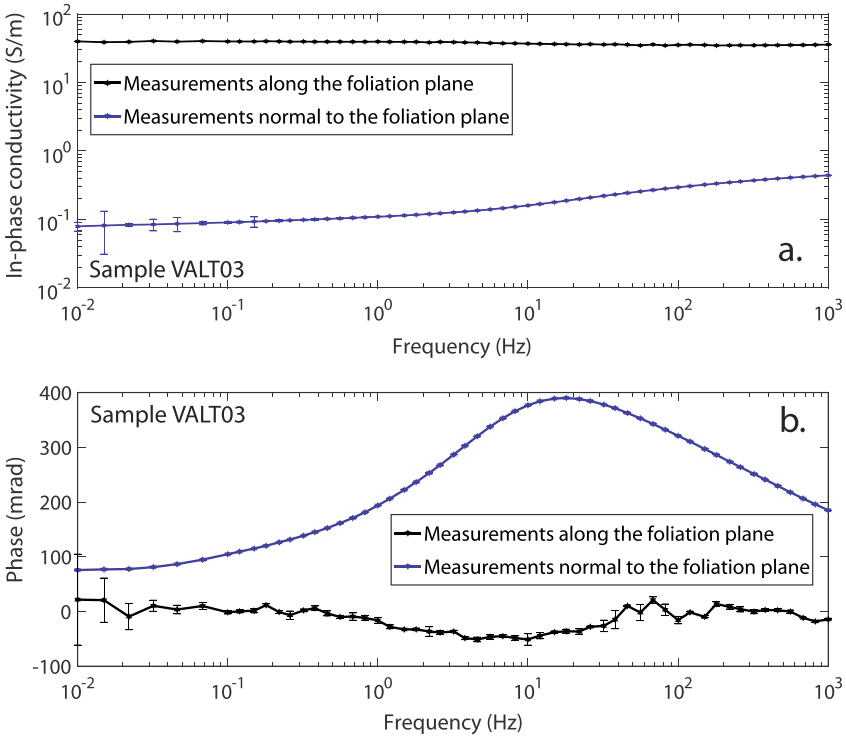

Figure 10. Spectral induced polarization of sample ValT3 (black schist). (a) In-phase conductivity spectra in the direction and normal to the foliation plane. (b) Phase spectra in the direction and normal to the foliation plane. Note the high conductivity and small polarization along the foliation plane. This is consistent with graphite above a percolation threshold in this direction. Note the low conductivity and high polarization normal to the foliation plane consistent with disconnected graphite in this direction.

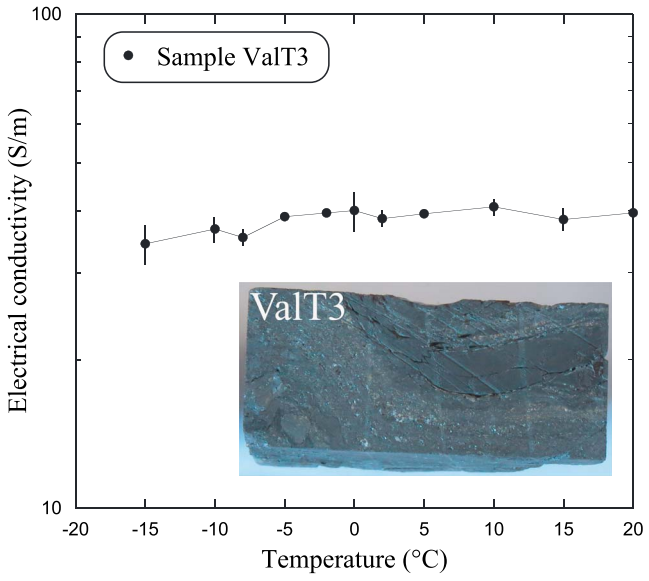

Figure 11. Electrical conductivity at 1 Hz of sample ValT3 (black schist) along the foliation plane. This sample exhibits an exceptionally high electrical conductivity (comprised between 30 and 40 S/m), quite temperature independent, and likely associated with graphite being above a percolation threshold through the core sample. The error bars are here determined from the uncertainty associated with the three cycles used at each frequency.

$$M_1 = \frac{9}{2}\varphi_m, \tag{18}$$

$$\sigma_1^\infty = 3\varphi_m \sigma_2^\infty. \tag{19}$$

Finally, from equations (18) and (19), we have

$$\sigma_1^0 = \sigma_1^\infty\left(1-\frac{9}{2}\varphi_m\right) = 3\varphi_m\left(1-\frac{9}{2}\varphi_m\right)\sigma_2^\infty. \tag{20}$$

The last parameter to obtain is the relaxation time τ_1 (in s). It is given by (Revil, Coperey, Mao, et al., 2018)

$$\tau_1 \approx \frac{a^2 e^2 C_m}{k_b T \sigma_2^\infty}, \tag{21}$$

where a denotes the diameter of the metallic particle (in m), C_m denotes the concentration of the charge carriers in the solid metallic particle (in m^{-3}), and e the elementary charge (1.6×10^{-19} °C).

2.4. Influence of Temperature and Permafrost

We discuss now the temperature dependence of the complex conductivity above the freezing temperature (typically but not necessarily around 0 °C). Following Vinegar and Waxman (1984), the pore water conductivity and mobilities B and λ have all the following linear temperature dependence:

Table 2
Sample ValT1a, Cole-Cole Parameters Resulted From Fitting the Laboratory Measurements With Double Cole-Cole Model

Temperature (°C)	σ_∞ (S/m)	M_1 (-)	M_{MW} (-)	c_1 (-)	c_{MW} (-)	τ_1 (s)	τ_{MW} (s)	RMS (%)
20	2.18E−03	0.569	0.278	0.67	0.21	9.81E−07	4.41E−07	2.72E−01
15	2.01E−03	0.581	0.275	0.70	0.21	1.13E−06	4.46E−07	2.86E−01
10	1.95E−03	0.588	0.285	0.74	0.22	1.12E−06	3.08E−07	3.03E−01
5	1.90E−03	0.663	0.228	0.67	0.20	7.54E−07	2.96E−07	2.73E−01
2	1.75E−03	0.617	0.277	0.70	0.20	1.05E−06	8.77E−08	3.07E−01
0	1.74E−03	0.651	0.250	0.74	0.22	9.75E−07	2.92E−07	2.52E−01
−2	7.24E−04	0.751	0.226	0.47	0.02	3.12E−06	1.08E−07	1.07E+00
−5	4.52E−04	0.528	0.360	0.52	0.31	1.16E−05	2.55E−07	1.56E+00
−8	2.99E−04	0.495	0.399	0.52	0.43	2.28E−05	2.09E−06	1.74E+00
−10	1.90E−04	0.477	0.410	0.53	0.67	8.99E−05	5.55E−06	1.92E+00
−15	1.43E−04	0.304	0.612	0.58	0.69	3.62E−04	6.19E−06	1.73E+00

$$\Theta(T) = \Theta(T_0)[1 + \alpha_T(T - T_0)], \tag{22}$$

where T_0 and T are the reference temperature (T_0 = 25 °C) and the temperature (in °C), respectively; $\Theta(T)$ corresponds to $\sigma_w(T)$, $B(T)$, or $\lambda(T)$; and $\Theta(T_0)$ corresponds to the same property at T_0, and the sensitivity α_T is in the range 0.019–0.022/°C (e.g., Revil et al., 2017). According to equation (22), the conductivity goes to zero at a temperature of −25 °C, remarkably close to the so-called eutectic temperature T_E close to −21 °C for NaCl. Actually the eutectic temperature is exactly predicted for $\alpha_T = 1/(T_E + T_0) = 0.0217$/°C. Reaching the eutectic temperature leads to the simultaneous crystallization of ice and salt. In equation (22), the temperature dependence of the pore water conductivity is controlled by the temperature dependence of the ionic mobilities of the cations and anions. Taking equations (9) and (10) (together with equation (22)) into equations (1)–(4), the temperature dependence of the complex conductivity (i.e., in-phase and quadrature conductivities) is therefore imposed by the thermal dependence of charge carrier mobilities.

Equations (2)–(4) need to show explicitly the dependence of the different properties with the water content. Assuming that the first and second Archie exponents are equal to each other, that is, $n = m$ (see Revil, 2013), and assuming the segregation of the salt in the liquid water phase, these equations can be written as

$$\sigma_2^\infty = \theta^{m-1}\left(\phi\sigma_w + \rho_g B\mathrm{CEC}\right), \tag{23}$$

$$\sigma_2^0 = \theta^{m-1}\left[\phi\sigma_w + \rho_g(B - \lambda)\mathrm{CEC}\right]. \tag{24}$$

Below freezing conditions, the water content of the liquid water is changing with the temperature according to a freezing curve. Duvillard et al. (2018) and Coperey et al. (2019) used an exponential freezing curve for the volumetric water content $\theta(T)$ written as

Table 3
Sample ValT1b, Cole-Cole Parameters Resulted From Fitting the Laboratory Measurements With Double Cole-Cole Model

Temperature (°C)	σ_∞ (S/m)	M_1 (-)	M_{MW} (-)	c_1 (-)	c_{MW} (-)	τ_1 (s)	τ_{MW} (s)	RMS (%)
20	1.00E−01	0.551	0.380	0.60	0.62	1.31E−02	8.34E−06	3.62E−01
15	9.99E−02	0.515	0.428	0.60	0.53	1.33E−02	6.17E−06	3.73E−01
10	9.98E−02	0.463	0.488	0.59	0.52	1.38E−02	4.35E−06	3.71E−01
5	9.93E−02	0.511	0.443	0.60	0.56	1.17E−02	9.45E−06	3.86E−01
2	9.51E−02	0.496	0.463	0.59	0.56	1.18E−02	6.53E−06	3.42E−01
0	9.99E−02	0.501	0.460	0.60	0.63	1.18E−02	9.27E−06	5.62E−01
−2	9.99E−02	0.515	0.449	0.59	0.64	1.12E−02	1.15E−05	3.38E−01
−5	9.17E−02	0.501	0.465	0.59	0.63	1.19E−02	9.97E−06	2.95E−01
−8	8.98E−02	0.459	0.514	0.59	0.76	1.20E−02	1.24E−05	3.22E−01
−10	7.61E−02	0.452	0.519	0.59	0.62	1.59E−02	1.34E−05	2.82E−01
−15	4.77E−02	0.455	0.515	0.61	0.49	2.55E−02	3.37E−05	2.73E−01

Table 4
Sample ValT2a, Cole-Cole Parameters Resulted From Fitting the Laboratory Measurements With Double Cole-Cole Model

Temperature (°C)	σ_∞ (S/m)	M_1 (-)	M_{MW} (-)	c_1 (-)	c_{MW} (-)	τ_1 (s)	τ_{MW} (s)	RMS (%)
20	2.47E−03	0.367	0.417	0.30	0.69	9.53E−04	2.92E−05	9.87E−02
15	2.31E−03	0.354	0.460	0.32	0.69	1.21E−03	2.56E−05	9.11E−02
10	2.00E−03	0.371	0.451	0.31	0.70	1.10E−03	3.12E−05	9.82E−02
5	1.86E−03	0.323	0.520	0.31	0.67	1.61E−03	2.43E−05	9.66E−02
2	1.67E−03	0.375	0.474	0.30	0.72	8.96E−04	2.80E−05	8.82E−02
0	1.55E−03	0.374	0.478	0.30	0.72	9.91E−04	2.93E−05	9.54E−02
−2	1.56E−03	0.321	0.550	0.31	0.69	1.39E−03	2.25E−05	9.64E−02
−5	1.14E−03	0.390	0.504	0.29	0.78	4.98E−04	2.84E−05	9.28E−02
−8	9.31E−04	0.412	0.497	0.28	0.78	3.06E−04	2.86E−05	9.96E−02
−10	8.18E−04	0.395	0.529	0.27	0.78	2.74E−04	2.74E−05	1.05E−01
−15	6.70E−04	0.332	0.613	0.27	0.79	2.76E−04	2.29E−05	1.10E−01

$$\theta(T) = \begin{cases} (\phi - \theta_r)\exp\left(-\frac{T - T_F}{T_C}\right) + \theta_r, & T \le T_F \\ \phi, & T > T_F \end{cases}, \tag{25}$$

which has the advantage to only require three parameters, T_F (the liquidus or freezing point), T_C (a characteristic temperature), and θ_r (the residual water content).

3. Laboratory Experiments

3.1. Core Sample Characterization

We consider in this study four samples from the French Alps (Val Thorens, ~2,850 m above sea level) and one sample from the Swiss Alps (Mont Fort, 3,328 m above sea level). Three of these samples are graphitic (black) schists (ValT1, ValT2, and ValT3) and two are graphitic tight sandstones (S1 and S2). The complex conductivity of the two graphitic schists (ValT1 and ValT2) was measured both normal to foliation plane (experiments labeled ValT1.a and ValT2.a) and along it (experiments labeled ValT1b and ValT2b). The samples are shown in Figure 3.

The samples were first dried for 24 hr at about 50 °C and then saturated under vacuum with NaCl solutions of known conductivity (σ_w = 0.019 S/m at 25 °C; see Woodruff et al., 2014, for additional details regarding this procedure). The core samples were left in this solution for two weeks to complete saturation. The complex conductivity spectra were obtained over the temperature range of +20 °C to −15 °C. The samples were put in a bag and immersed in a thermally controlled bath (Kiss K6 from Huber). For each experiment, sample and bath temperatures were recorded every minute with thermocouples in contact with the core sample and one sensor placed directly in the bath. We use K-thermocouples and a data logger CR1000 from Campbell scientific for the thermal monitoring.

Table 5
Sample ValT2b, Cole-Cole Parameters Resulted From Fitting the Laboratory Measurements With Double Cole-Cole Model

Temperature (°C)	σ_∞ (S/m)	M_1 (-)	M_{MW}(-)	c_1 (-)	c_{MW} (-)	τ_1 (s)	τ_{MW} (s)	RMS (%)
20	3.92E−03	0.485	0.164	0.84	0.54	3.87E−02	6.55E−04	7.05E−01
15	2.70E−03	0.438	0.155	0.87	0.53	4.32E−02	5.03E−04	8.51E−01
10	2.01E−03	0.425	0.184	0.84	0.48	5.52E−02	1.93E−04	7.52E−01
5	1.48E−03	0.400	0.220	0.81	0.44	7.61E−02	8.95E−05	6.40E−01
2	1.24E−03	0.407	0.202	0.80	0.47	9.49E−02	8.19E−05	5.24E−01
0	1.14E−03	0.388	0.239	0.78	0.45	1.10E−01	3.28E−05	4.52E−01
−2	9.83E−04	0.420	0.212	0.77	0.59	1.31E−01	7.06E−05	3.05E−01
−5	8.13E−04	0.362	0.329	0.77	0.44	1.87E−01	5.24E−05	1.81E−01
−8	5.00E−04	0.445	0.202	0.75	0.61	2.41E−01	4.05E−04	1.60E−01
−10	3.97E−04	0.495	0.142	0.73	0.80	2.71E−01	1.04E−03	3.93E−01
−15	2.24E−04	0.492	0.155	0.72	0.82	4.66E−01	1.88E−03	5.67E−01

Table 6
Sample Sandstone 1 (S1), Cole-Cole Parameters Resulted From Fitting the Laboratory Measurements With Double Cole-Cole

Temperature (°C)	σ_∞ (S/m)	M_1 (-)	M_{MW} (-)	c_1 (-)	c_{MW}(-)	τ_1 (s)	τ_{MW} (s)	RMS (%)
20	3.45E−04	0.255	0.359	0.27	0.82	1.03E−03	1.30E−05	9.89E−02
15	2.95E−04	0.221	0.398	0.29	0.75	2.74E−03	1.26E−05	9.61E−02
10	2.55E−04	0.198	0.426	0.30	0.71	5.05E−03	1.38E−05	1.26E−01
5	2.28E−04	0.201	0.452	0.29	0.74	3.77E−03	1.28E−05	1.14E−01
2	1.98E−04	0.219	0.426	0.28	0.77	3.41E−03	1.76E−05	1.13E−01
0	1.81E−04	0.252	0.392	0.27	0.82	1.69E−03	2.18E−05	1.58E−01
−2	1.60E−04	0.234	0.390	0.29	0.80	3.00E−03	2.55E−05	1.95E−01
−5	8.85E−05	0.171	0.569	0.33	0.81	5.13E−03	2.58E−05	2.52E−01
−8	5.89E−05	0.232	0.555	0.28	0.88	1.02E−03	3.85E−05	2.59E−01
−10	5.62E−05	0.360	0.483	0.23	0.93	2.19E−05	3.99E−05	2.69E−01
−15	3.65E−05	0.320	0.576	0.23	0.91	1.63E−05	4.24E−05	4.65E−01

Furthermore, the porosity and CEC of the core samples were obtained for all the core samples (see Table 1). The CEC was measured with the cobalthexamine method (Aran et al., 2008; Ciesielski et al., 1997). Low values of CEC were obtained indicating the absence of clay materials in the core samples.

To better understand the source of the observed electrical behavior of these samples, we have characterized the microstructural arrangement of graphite within samples ValT1 and ValT2. Standard polished thin sections of the samples were examined using transmitted and reflected light optical, and electron microscopic methods (see also Kirilova et al., 2017). The latter employed a Zeiss Sigma FE-SEM operating at 8.5-mm working distance and 15-keV accelerating voltage at Otago University's Microscale and Nanoscale Imaging Unit. Images were obtained in secondary electron and backscattered electron modes. Chemical maps of selected areas were also obtained using an Oxford Instruments EDS detector and Aztec software.

The element maps (Figures 4a–4d) demonstrate that the phase that resembles graphite in hand specimen and optical microscope is indeed composed of carbon. They also highlight the dominance of quartz and chlorite in pressure fringes. However, because they are not quantitative we cannot precisely define the mineralogy of the phyllosilicates from them. The distribution of graphite in the samples is bimodal. Mode 1 graphite grains (Figures 4g and 4h) are approximately 250 μm in diameter and euhedral. They are aggregated in isoclinally folded pods, surrounded by quartz and chlorite pressure fringes. Mode 2 graphite (Figures 4i and 4j) grains are much smaller, less than tens of micrometers, and individual grains are elongated and spread along foliation. The total area of Mode 2 graphite appears to be less than that of Mode 1 graphite. There may be a genetic relationship between these two graphite modes but the microstructural information we have is not sufficient to determine which phase is the "parent." Nevertheless, the impact of the two graphite modes on the electrical properties of the rock is expected

Table 7
Sample Sandstone 2 (S2), Cole-Cole Parameters Resulted From Fitting the Laboratory Measurements With Double Cole-Cole

Temperature (°C)	σ_∞ (S/m)	M_1 (-)	M_{MW} (-)	c_1 (-)	c_{MW} (-)	τ_1 (s)	τ_{MW} (s)	RMS (%)
20	1.29E−03	0.146	0.489	0.45	0.86	7.80E−03	1.61E−06	3.61E−01
15	9.10E−04	0.170	0.402	0.45	0.88	9.29E−03	2.62E−06	2.85E−01
10	8.40E−04	0.155	0.452	0.46	0.83	1.11E−02	2.00E−06	2.62E−01
5	6.76E−04	0.157	0.435	0.46	0.79	1.32E−02	1.61E−06	2.29E−01
2	6.03E−04	0.154	0.439	0.48	0.76	1.69E−02	1.70E−06	2.44E−01
0	5.56E−04	0.155	0.442	0.48	0.74	1.79E−02	1.79E−06	2.23E−01
−2	4.92E−04	0.164	0.418	0.48	0.75	1.95E−02	2.33E−06	2.42E−01
−5	2.64E−04	0.124	0.563	0.48	0.80	3.11E−02	3.18E−06	3.11E−01
−8	2.36E−04	0.095	0.680	0.46	0.88	4.30E−02	4.37E−06	4.26E−01
−10	1.78E−04	0.098	0.675	0.46	0.81	4.68E−02	3.83E−06	3.64E−01
−15	2.36E−04	0.095	0.680	0.46	0.88	4.30E−02	4.37E−06	4.26E−01

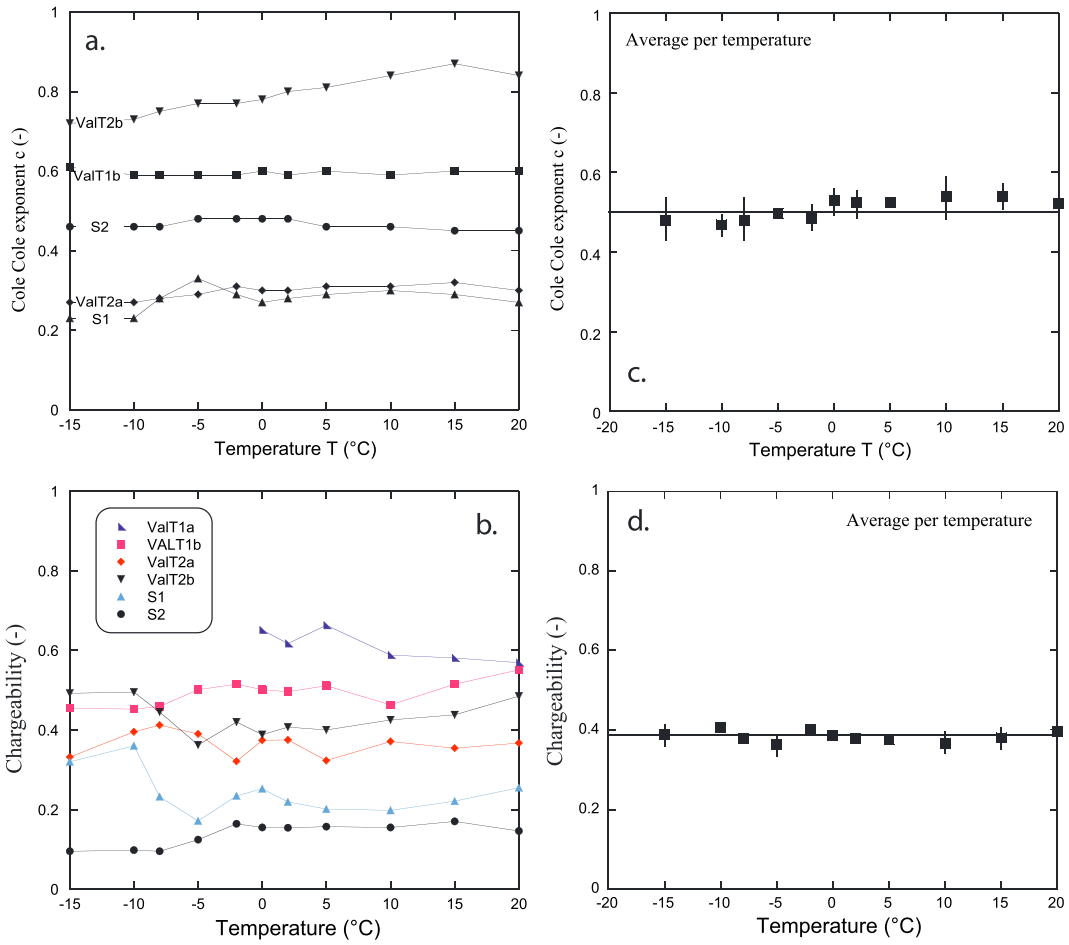

Figure 12. Cole-Cole parameters versus temperature. (a) Cole-Cole exponent c_1 versus temperature for various samples of the data set. Note that the Cole-Cole exponent is essentially independent of the temperature in agreement with the prediction of the model. (b) Chargeability M versus temperature for various samples of the data set. The chargeability appears essentially independent of the temperature in agreement with the prediction of the model. (c) Average of the Cole-Cole exponent c_1 versus temperature. This demonstrates that in average, the Cole-Cole exponent c_1 is temperature of temperature. (d) Average of the chargeability versus temperature. This demonstrates that in average, the chargeability is temperature of temperature.

to be quite different with Mode 2 expected to polarize at higher frequencies (see equation (21)), possibly above the range investigated in the present study. This could be investigated in future studies by very broadband spectroscopy. Mode 1 grains, although volumetrically dominant, are isolated from one another, and have a low surface area per volume ratio. Conversely, Mode 2 graphite grains are more likely to form linked, through going networks and have substantial surface area compared to their volume.

Raman spectra were also measured by an Alpha 300R+ confocal Raman microscope (WITec, Ulm, Germany) with a 532-nm laser (Coherent, Santa Clara, CA), located at the Department of Chemistry, University of Otago, New Zealand. The spectra were calibrated using the Raman band from a silicon wafer prior to each set of measurements. The laser (5.0 mW) was focused on the samples with a 50X Zeiss objective. The scattered light was dispersed with a 1,200-g/mm grating. The integration time of each Raman spectrum was 2 s with 20 co-additions. The spectra were preprocessed in Grams AI 9.1 (Thermo Fisher Scientific Inc.), and then peak fitting of three Lorentzian functions to each spectrum was performed on MATLAB (Figure 5). For each spectrum, the area ratio (known as crystallinity index) was calculated by using the equation $R_2 = A_{D1}/(A_{D1} + A_G + A_{D2})$, where Ai is the area of the ith peak, G band is

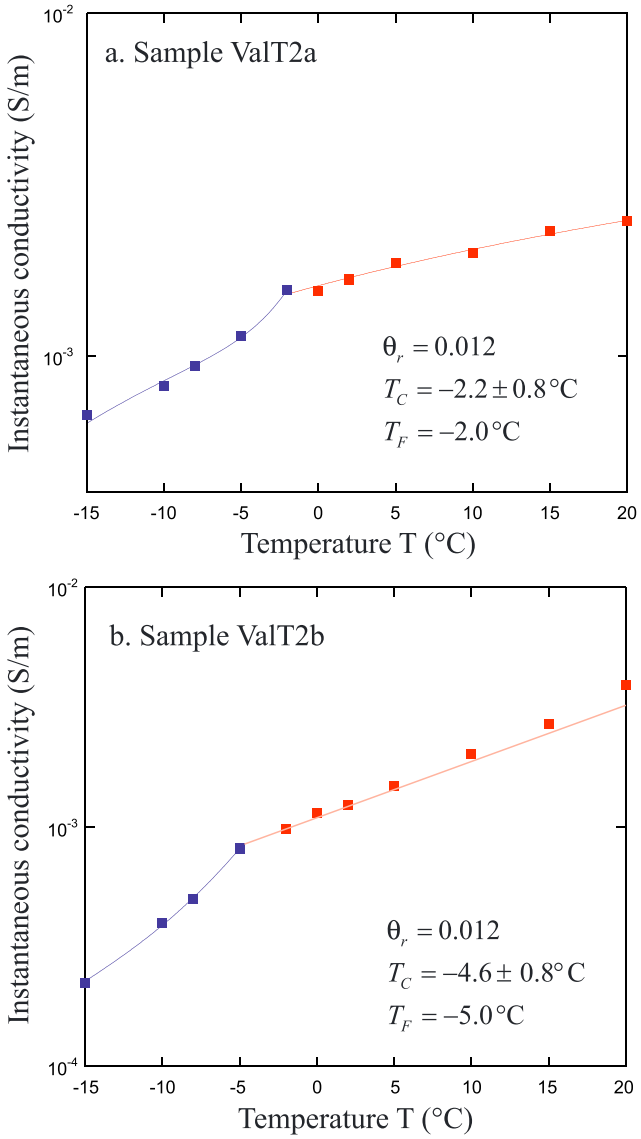

Figure 13. Instantaneous conductivity versus temperature for sample ValT2. (a) Transverse component. The instantaneous conductivity at 25 °C is equal to 0.0027 ± 0.0001 S/m and $\alpha_T = 0.016 \pm 0.001$/°C. (b) In-plane component. Note that the red curve is linear in a linear-linear space representation of the data. The instantaneous conductivity at 25 °C is equal to 0.0041 ± 0.0001 S/m and $\alpha_T = 0.024 \pm 0.004$/°C.

the main high-frequency band of graphite, and D1 and D2 bands are the defect bands observed in the first-order Raman spectrum of graphite (Wopenka & Pasteris, 1993). Furthermore, maximum metamorphic temperatures were estimated in the range 330–640 °C by the linear correlation $T(°C) = -445\ R_2 + 641 \pm 50$ °C (Beyssac et al., 2002). All Raman spectra show typical graphite bands at ~1,580 (G), 1,350 (D1), and 1,620 (D2) cm. Representative Raman data from five spectra lead to maximum metamorphic temperatures in the range 312 to 371 °C. Spectrum 2 is shown in Figure 5. The R_2 values range from 0.606 to 0.740, indicating low graphite crystallinity. The experienced maximum metamorphic temperature for this spectrum is estimated to be 371 °C.

3.2. Complex Conductivity Spectra

Complex conductivity measurements were carried out from positive to negative temperatures. At each temperature and before the electrical measurements, the sample was left for 3 to 10 hr to reach electrical and

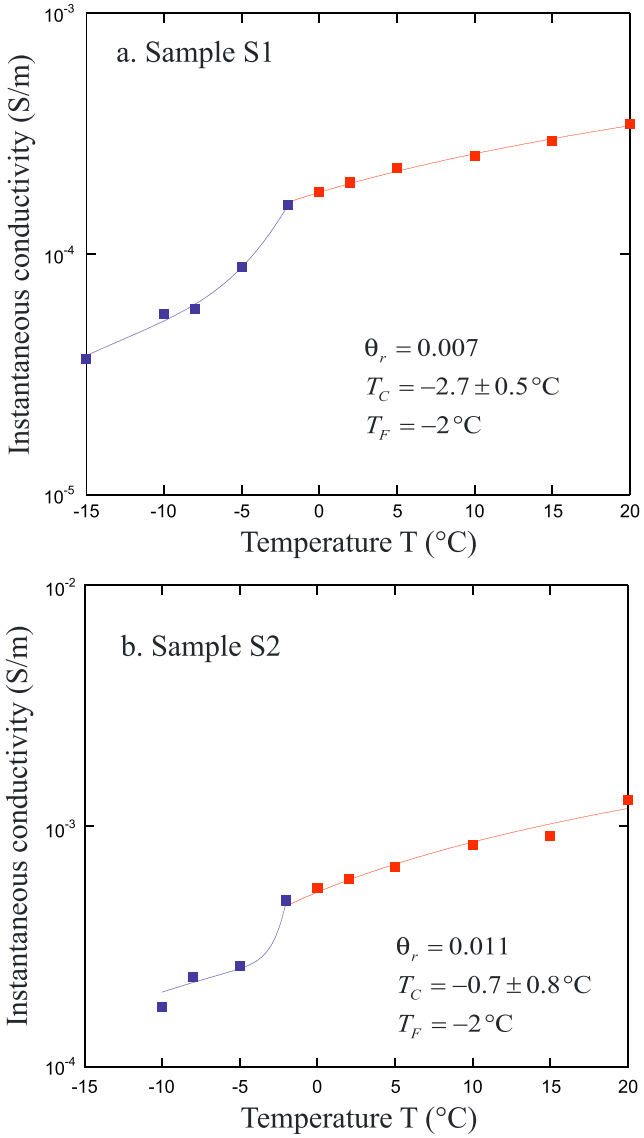

Figure 14. Instantaneous conductivity versus temperature. (a) Sample S1. The instantaneous conductivity at 25 °C is equal to 0.00038 ± 0.00007 S/m and $\alpha_T = 0.021 \pm 0.001$/°C. (b) Sample S2. Note that the red curve is linear in a linear-linear space representation of the data. The instantaneous conductivity at 25 °C is equal to 0.00135 ± 0.00001 S/m and $\alpha_T = 0.024 \pm 0.002$/°C.

thermal equilibria. Complex electrical conductivity measurements were carried out with a high-precision impedance analyzer ZEL-SIP04-V02 (Zimmermann et al., 2008, Figure 6, the temperature-controlled bath is also shown in this figure). Resistance and phase shift were measured in the frequency range of 0.01 Hz to 45 kHz with an imposed voltage of 1 V. A complete experiment for one core sample (in one direction) over the temperature and frequency ranges discussed above takes about one week. An additional set of measurements were performed for sand/graphite mixes at the following volume fractions of graphite 0.20, 0.17, 0.061, 0.06, 0.051, 0.028, and 0.010. The chargeability versus graphite content is shown in Figure 6c confirming equation (18). For this figure, the chargeability is calculated using the difference in the in-phase conductivity between 10 kHz and 10 mHz).

3.3. Results

Figures 7–9 display the frequency dependence of the in-phase and quadrature conductivity at different temperatures. The error bars (not shown on the figures) are known and determined, for each measurement, over

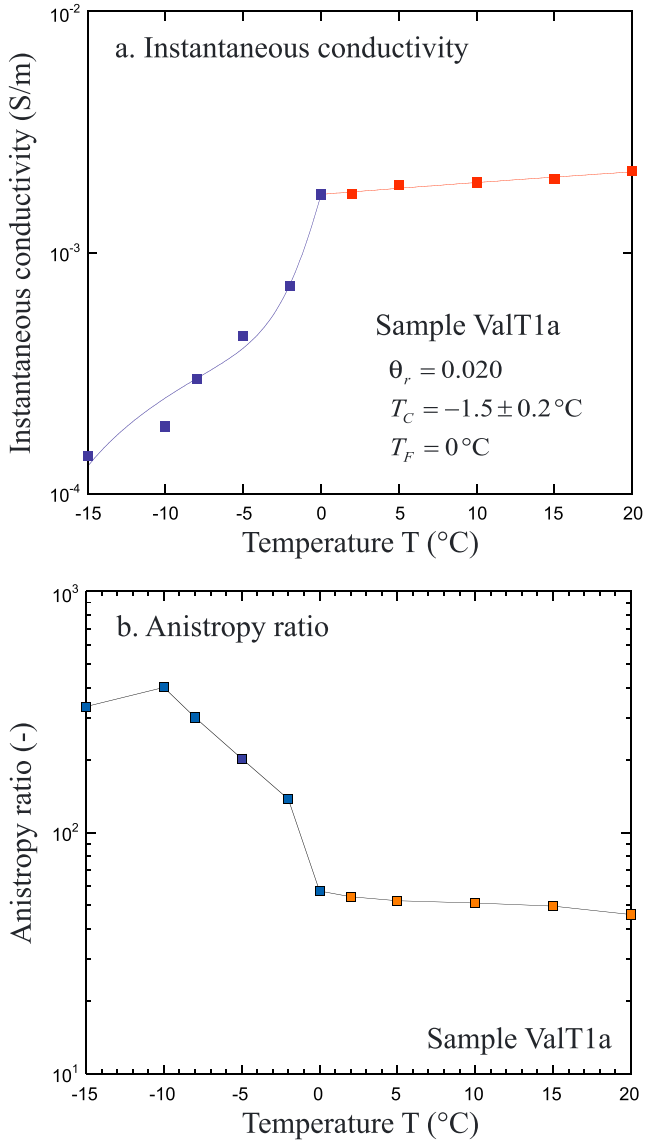

Figure 15. (a) Instantaneous conductivity versus temperature for Sample ValT1a. Note the strong change in the conductivity versus temperature trend below the freezing point. Note that the red curve is linear in a linear-linear space representation of the data. The instantaneous conductivity at 25 °C is equal to 0.00226 ± 0.00004 S/m and $\alpha_T = 0.009 \pm 0.001$/°C. (b) Anisotropy ratio between the in-plane (foliation) instantaneous conductivity and the out-of-plane (normal to foliation) conductivity component. Note that the anisotropy ratio increases substantially below the freezing point. The line is just a guide to the eyes.

three cycles, at each frequency. They typically are smaller than 1% except for high frequencies above 100 Hz or 1 kHz. These values are not taken for the fit as shown in the graph. The measured phases are high (typically between 80 and 600 mrad at the peak frequency). For the two sandstones S1 and S2, the complex conductivity spectra are shown in Figure 7. In fact, clean sandstones (i.e., without minerals or semiconductors or clay) have generally weak polarization because of their low cation exchange capacity (Revil, Coperey, Deng, et al., 2018). At the opposite, the two sandstones investigated in this study exhibit very high quadrature conductivity (and therefore polarization) and chargeability (as discussed below). This high polarization is explained by the presence of a small percentage of graphite. Using equation (15), the volume fraction of graphite is about 5.7% vol. fraction for sandstone S1 and 3.25% vol. fraction for sandstone S2.

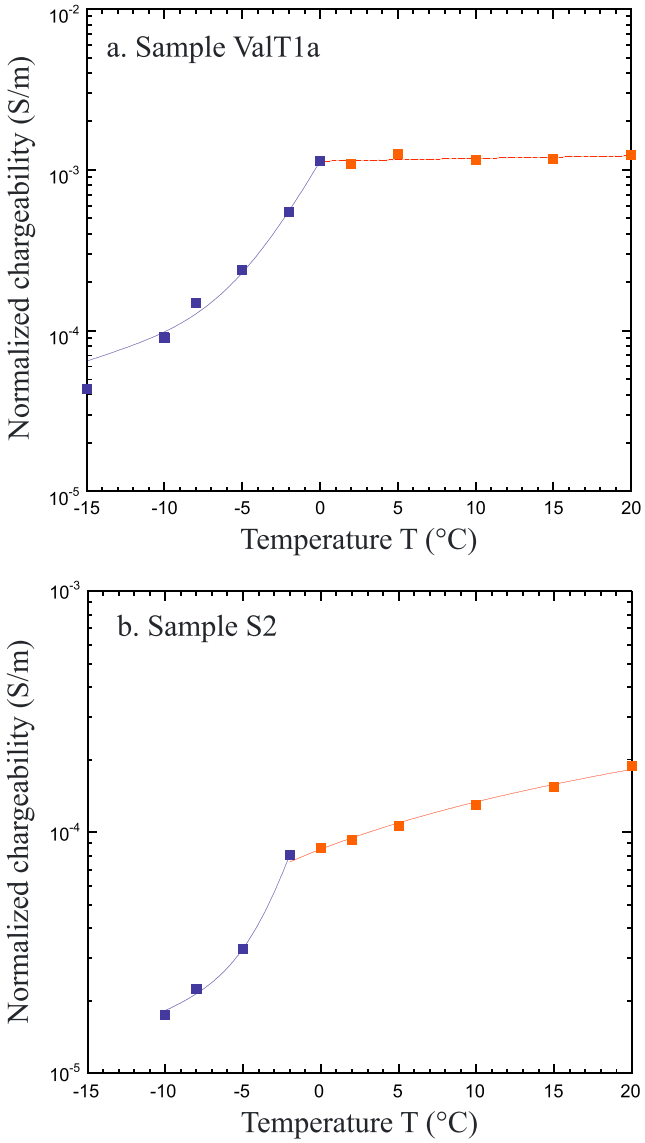

Figure 16. Normalized chargeability versus temperature. (a) Sample ValT1a. (b) Sample S2.

Figures 8 and 9 display the measurements normal to the foliation plane and the measurements parallel to the foliation plane for the two schist samples ValT2 and ValT1, respectively. These figures show the high dependence of the complex conductivity on temperature, especially in case of measurements normal to the foliation plane. Sample ValT1 exhibits a strong anisotropy. High values of the in-phase and quadrature conductivity are measured in the direction of the foliation plane. The high anisotropy is a result of the strongly marked foliation of this sample (see Figures 3 and 4). From the measured quadrature conductivity, we notice that the polarization phenomenon in this sample is high. Sample ValT2 shows a smaller degree of anisotropy than ValT1. However, this is consistent with the fact that the foliation appears less pronounced for this sample compared to ValT1 (Figure 4).

Sample ValT3 is very rich in graphite with a marked foliation. Its electrical conductivity was found to be extremely high (in the range 30 and 40 S/m). The phase could not be measured because its magnitude was below the sensitivity of the impedance meter. This is not surprising since the phase is approximately given by the ratio of the quadrature conductivity by the in-phase conductivity, and therefore, for a very high value of the in-phase conductivity (and possibly a small value of the quadrature conductivity), the phase is

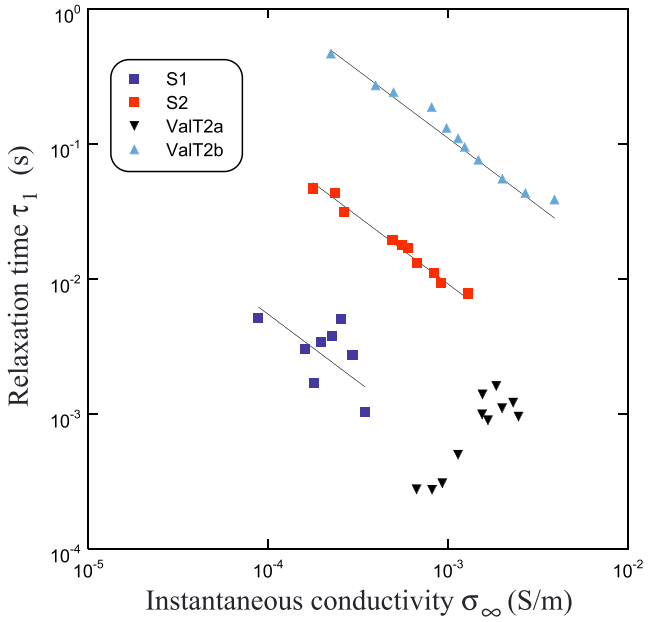

Figure 17. Low-frequency relaxation time versus instantaneous conductivity. The plain lines show the inverse relationship between the two parameters. The plain lines correspond to the fit using equation (26). For Sample ValT2a, the distribution of the grain sizes is too broad to determine correctly the position of the relaxation peak.

expected to be very small. Figure 10 shows the in-phase conductivity and the phase for Sample ValT3 (parallel and normal to foliation) as a function of frequency. Note the high conductivity and small polarization along the foliation plane. Normal to the foliation plane, the situation is the opposite. We observe indeed a much smaller conductivity by comparison with the conductivity of the foliation plane and a much stronger polarization (Figure 10). Both observations are consistent with disconnected graphite in the direction normal to the foliation plane. Figure 11 shows the in-phase conductivity measured parallel to foliation at 1 Hz as a function of temperature. The high conductivity and absence of polarization in the foliation plane are likely due to the high percentage of graphite above a percolation threshold in this direction. For this sample, the only explanation is that some of the graphite is connected through the entire core sample along the foliation plane. We postulate that for sample ValT3, the Mode 2 graphite grains form a network of continuous electronic conductors able to explain the anomalous high conductive behavior of this core sample along the foliation plane.

3.4. Analysis of the Cole-Cole Parameters

We use the approach described in Appendix A to fit the data. Tables 2–7 show Cole-Cole parameters resulted from fitting the measured complex conductivity with double Cole-Cole model (Appendix A). There are three polarization mechanisms in total. The first is associated with the nonmetallic grains, the second with graphite, and the third with the Maxwell-Wagner polarization. That said, in our case, the presence of graphite dominates the background polarization so only a double Cole-Cole model is used to fit the data. Therefore, the first response comes from the polarization of graphite, while the second response (or the second peak on the quadrature conductivity or the phase) comes from the Maxwell-Wagner polarization and possibly the spurious electromagnetic and capacitive effects (Abdulsamad et al., 2016).

Both the chargeability M_1 and the Cole-Cole exponent c_1 are independent of temperature (Figures 12a and 12b). This is in agreement with the model. The values of M_1 and $c_1$vary around an averaged value with small standard variation (Figures 12c and 12d). Actual changes in the chargeability M_1 and Cole-Cole exponent c_1 with temperature are very small and do not show clear trends with temperature. This is noticed for all samples tested in this study. Figures 13–15a show the temperature dependence of instantaneous conductivity, and Figure 15b shows how the anisotropy of sample ValT1 changes with temperature. We see clearly the two distinct trends above and below the freezing point T_F. These two trends are fitted by equations (22) and (25), respectively. The mean value of the sensitivity coefficient α_T is ~0.020/°C (as expected). The residual water content and the two fitted temperatures T_C and T_F are reported in Figures 13 and 14. Figure 15b shows that sample ValT1 is characterized by a substantial anisotropy above the freezing temperature (with an isotropy ratio around 40 to 60). This anisotropy ratio is rather temperature independent (as expected) above the freezing temperature. That said, the anisotropy ratio increases substantially below the freezing point to reach values >300. This observation could be explained as follow. The instantaneous conductivity normal to foliation goes down, presumably due to the high resistivity of ice as whatever pore fluid is present freezes. In contrast, parallel to foliation the primary conduction must be through graphite and is not significantly affected by freezing. Figure 16 shows the behavior of the normalized chargeability versus the temperature. As expected from the model, the same type of behavior is expected for the normalized chargeability by comparison with the instantaneous conductivity.

The relaxation time is plotted as a function of the instantaneous conductivity in Figure 17. In agreement with the model, the trends exhibit an inverse relationship between the two parameters. Indeed, if we combine equations (16) and (21), we obtain

Table 8
Parameters Used for Finite Element Simulation

Parameter	Value
$D_{(-)}$	1.7×10^{-9} m^2/s
$D_{(+)}$	1.1×10^{-9} m^2/s
$D^m_{(+)} = D^m_{(-)}$	2.9×10^{-5} m^2/s
$C^m_{(+)} = C^m_{(-)}$	2.8×10^{22} m^{-3}
T_0	298 K
ε_0	8.81×10^{-12} F/m
ε_S	10.9 ε_0
ε_w	80 ε_0
ϕ	0.5, 0.1, 0.01
θ_r	0.002
T_F	0 °C
T_C	−1.5 °C
a	500 μm

Note. The quantity $C^m_{(\pm)}$ denotes the charge concentration in the semiconductor grain at equilibrium state, $D^m_{(\pm)}$ denotes the diffusion coefficients of the charge carriers in the metallic particle, $D_{(\pm)}$ denotes the diffusion coefficients of cations and anions in the solution, and ε_0, ε_S, and ε_w denote the permittivity of free space, the permittivity of the metallic grain, and the permittivity of electrolyte, respectively (their temperature dependence is small and neglected). The quantity ϕ denotes the porosity of the background, while T_F and T_C denote the two temperatures in the exponential freezing law (see equation (25)). The instantaneous conductivity of the metallic grain is 10 S/m (at 25 °C) while the pore liquid conductivity is 1 S/m at 25 °C. The quantity a denotes the diameter of the metallic particle.

$$\tau_1 \approx \frac{a^2 e^2 C_m (1 + 3\varphi_m)}{k_b T \sigma_\infty}. \quad (26)$$

The inverse relationship between the relaxation time and the conductivity of the background makes the relaxation time increase with decreasing the temperature (not shown here). There is however one of the four samples (ValT2a) that does not show this trend. In fact, for broad grain size distribution, it becomes difficult to identify the peak of the phase and therefore the Cole-Cole relaxation time. In addition, for small grain sizes, the phase peak is occurring at high frequencies and may be covered up by different other mechanisms (Abdulsamad et al., 2016). This seems to be the case for this rock sample.

3.5. Numerical Modeling

We use here the approach initially developed in Abdulsamad et al. (2017) to see if we can explain the observed response of the Cole-Cole parameters as a function of temperature. This approach was used by Revil, Coperey, Mao, et al. (2018) to successfully model the effect of the temperature of a porous material with a metallic inclusion above the freezing temperature. In the present case, we treat graphite as a semiconductor (e.g., Slonczewski & Weiss, 1958). For large grain (>500 μm), the influence of charge diffusion outside the metallic particle is small and is therefore neglected in the numerical model (see Revil, Coperey, Mao, et al., 2018, for details). In freezing conditions (the icing point is typically reached between 0 °C and −4 °C in our experiments; see Figures 13–15), the complex conductivity response is expected to change because of the change in the liquid water content in the material. We performed simulations of the polarization phenomena in presence of a grain of graphite of conductivity 10 S/m. The metallic grain is immersed in a background porous material with a pore water conductivity of 1 S/m (at 25 °C). The simulation was performed at different temperatures in the range +30 °C to −18 °C and at three different porosities (0.01, 0.1, and 0.5). We use

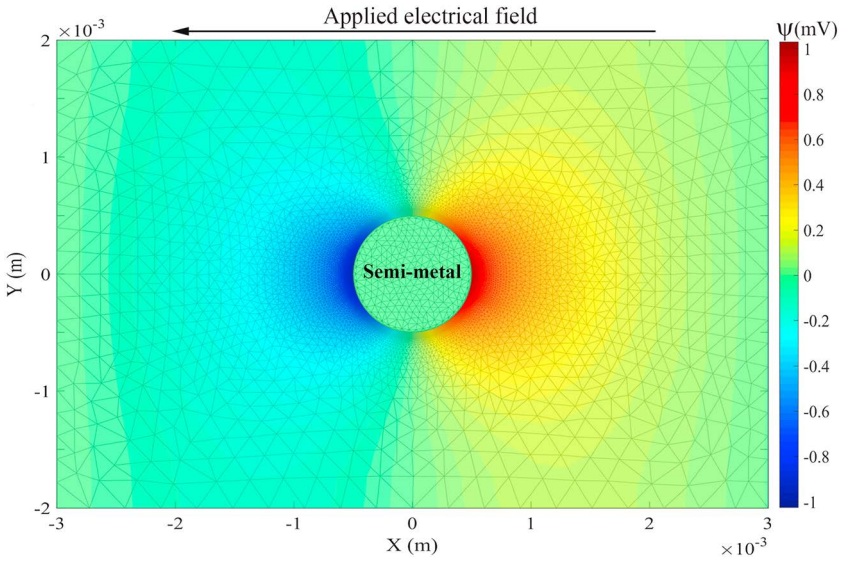

Figure 18. Distribution of the secondary potential associated with a metallic particle embedded into a conductive (nonpolarizable) background material. This computed secondary potential is similar to that sketched in Figure 2b. The polarization is coming from the metallic particle itself (i.e., the background is here nonpolarizable). The parameters used are those of Table 8. The simulations are performed for a range of temperatures.

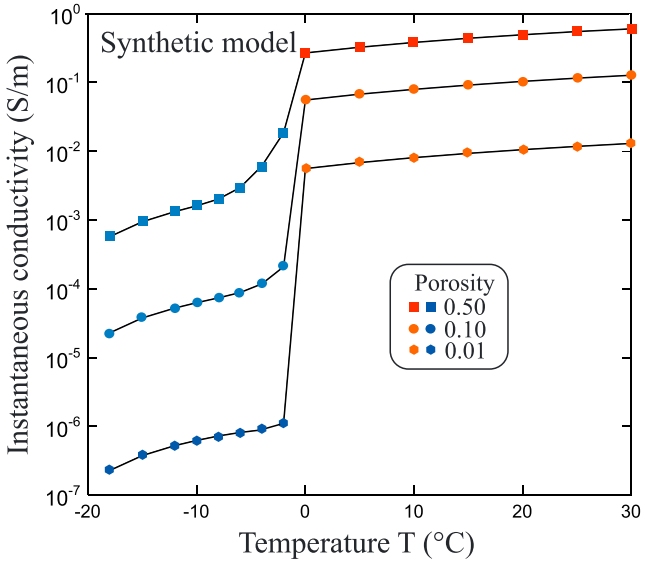

Figure 19. Instantaneous conductivity versus temperature for the synthetic case. The parameters used are those of Table 8 (compare with Figures 14, 15a, and 16).

equations (22) and (25) to model the effect of the temperature upon the background conductivity. The parameters used for the numerical (finite element) simulations are reported in Table 8. The numerical results are similar to that found for sample ValT1.

A typical simulation of the secondary electrical potential distribution associated with the presence of the metallic particle in its host is shown in Figure 18. The results of the numerical simulations are presented in the Figures 19 and 20. In Figure 19, the instantaneous conductivity is shown as a function of temperature showing the same trend as in the laboratory experiments (decrease of the instantaneous conductivity with decreasing temperature). In Figure 20, the relaxation time appears inversely proportional to the instantaneous conductivity. The results of the numerical simulation are therefore consistent with the experimental results: (1) the instantaneous conductivity decreases with the decrease of the temperature at low temperatures and (2) the product of the Cole-Cole relaxation time with the instantaneous conductivity is nearly constant. The chargeability M and the exponent c (not shown here) are independent on temperature.

4. Field Work

In order to show how the previous results can be applied to real data, we analyze in this section two electrical conductivity and induced polarization profiles obtained over an area of recognized permafrost and graphitic schists (Duvillard et al., 2018) in the ski resort of Val Thorens in the French Alps (Figures 21a and 21b). This area is known to be rich in coal and graphite (Aillères, 1996; Fabren, 1958). The multiple gradient array (Dahlin & Zhou, 2006) was used to acquire the resistivity and chargeability data sets with a protocol comprising 212 quadrupoles per profile. Each profile has 32 electrodes with a 20-m electrode spacing between consecutive electrodes. Stainless steel electrodes were used for both current injection and voltage measurements. In order to avoid the electrode polarization problem and to minimize electromagnetic coupling effects, we separated the electrodes used for current injection from those used for measuring the potential using the two cables technique proposed by Dahlin et al. (2002) (see also Dahlin & Leroux, 2012). The measurements were carried out using an ABEM SAS4000 (four-channel resistivity meter) and in-house built protocol. The injected current is of the pseudocontinuous type (+I, 0, −I, 0) with 1 s of current injection and 1 s for voltage measuring (I denotes the injected current in A).

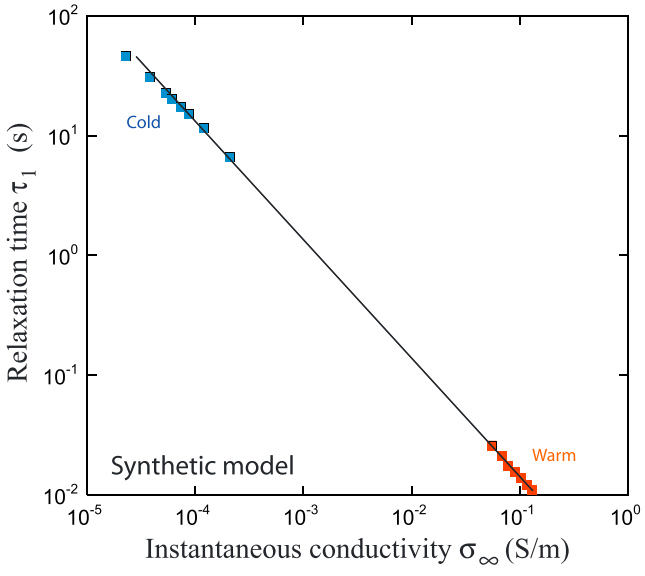

Figure 20. Relaxation time versus instantaneous conductivity for the synthetic case corresponding to a porosity of 0.10. The parameters used are those of Table 8. The plain line indicates that the relaxation time is inversely proportional to the instantaneous conductivity. This synthetic modeling is therefore consistent with the laboratory experiments (Figure 17).

Ten partials chargeabilities were recorded during the monitoring time to get the apparent chargeability M used in the study. The measurements were carried out in the summer 2018 and no issue was found with the contact resistances. Figure 22 shows the typical decay of the secondary voltage (here expressed in terms of apparent chargeabilities). For the chargeability inversion, only the first window was used.

The inversion of the field data was performed using the commercial software Res2dinv (Loke, 2002; Loke & Barker, 2004). The results are shown in Figure 23 for Profile P1 and in Figure 24 for Profile P2. The permafrost is shown as a poorly conductive area (conductivity in the range 10^{-4} to 10^{-5} S/m) and low normalized chargeability (in the range 10^{-5} to 10^{-7} S/m). The chargeability distributions for the two profiles are shown in Figure 25. As shown in Figure 12a, chargeability does not depend on temperature and is essentially a function of the content in graphite (see Figure 5c). Figure 26 summarizes the relationship between the normalized chargeability and the (instantaneous)

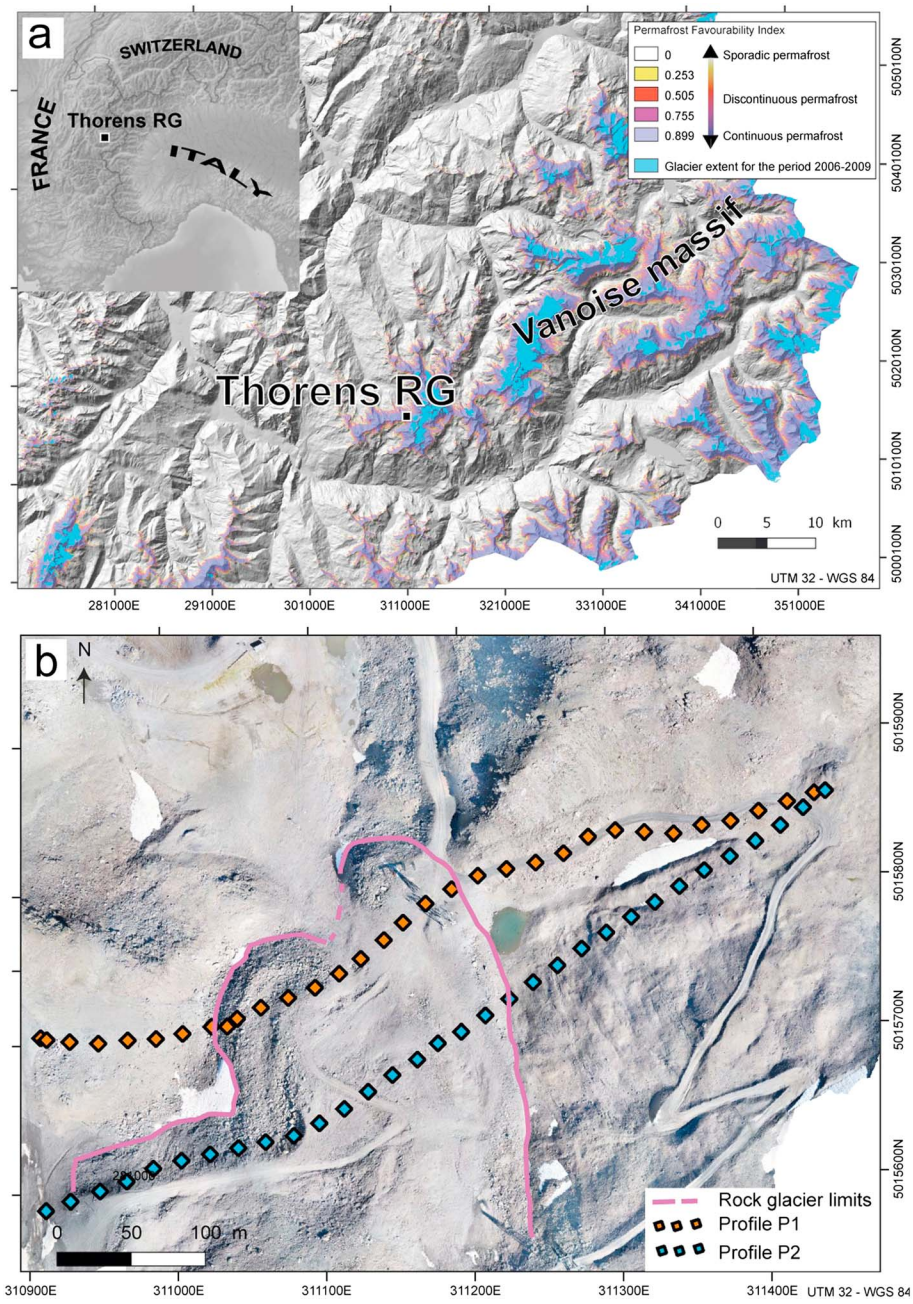

Figure 21. (a) Localization of the Thorens rock glacier (RG) located in the Vanoise massif (French Alps, Institut Géographique National, 25-m digital elevation map with glacier extent for the period 2006–2009 made thanks to the work of Gardent et al. (2014) and Permafrost Favorability Index from the work of Marcer et al. (2017)). (b) Map of the test site with the Thorens rock glacier test site. The map shows the location of the two electrical resistivity and induced polarization profiles P1 and P2 (20-m spacing between the electrodes) and the limits of the rock glacier.

conductivity. Above the value of $M = R = 0.08$ (highest value reached for nonmetallic rocks), the data can only be explained by the presence of graphite. In absence of graphite, we observe that the chargeability (i.e., the ratio between the normalized chargeability and the conductivity) is close to R indicating the strong role of surface (double layer) conductivity on the overall conductivity response as discussed in Duvillard et al. (2018). The background is characterized by a chargeability of 0.03. Figure 26 shows also the effect of the lithology and temperature on both the conductivity and normalized chargeability.

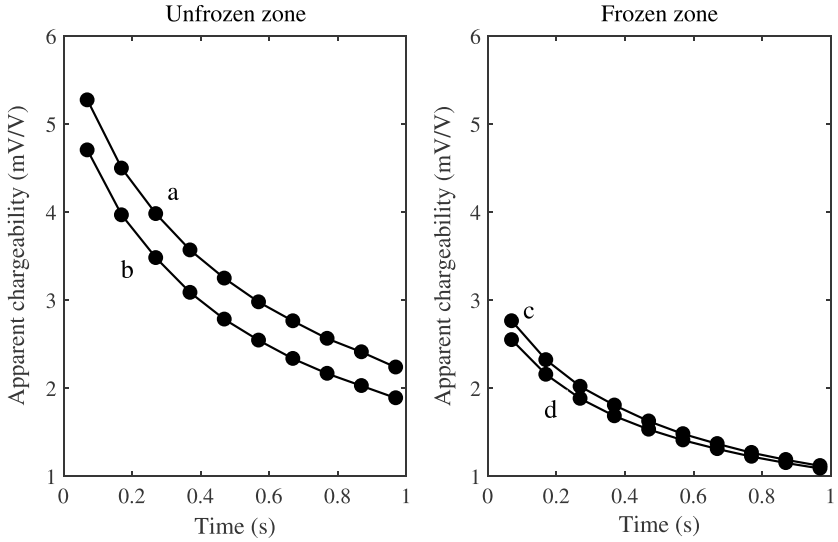

Figure 22. Apparent chargeability decay curves over the frozen and unfrozen zones. The exponential decay type of the curve is generally (but not necessarily) a good indicator of data quality. The labels a to d indicate the position of some specific quadripoles used for the measurements.

Using equation (15), we can now use the chargeability data of the tomograms shown in Figure 25 with the background chargeability of 0.03 (Figure 26) to image the volume content of graphite (Figure 27). The volume content of graphite reaches a maximum of 2.5%, which is compatible with the amount of graphite in the core samples. The present approach illustrates how the graphite content can be imaged in this type of Alpine environments with or without the presence of permafrost.

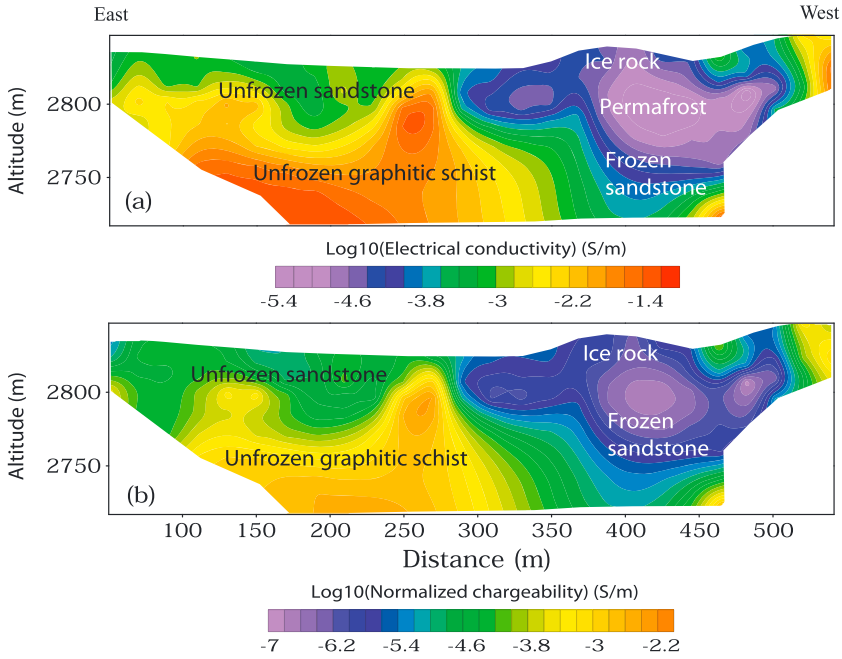

Figure 23. Large-scale electrical conductivity and normalized chargeability tomograms crossing the area of interest (Profile P1). (a) Electrical conductivity tomogram showing position and depth of the permafrost (about 70 m). (b) Normalized chargeability tomogram for which the high normalized chargeability zones correlate with graphitic schist formations.

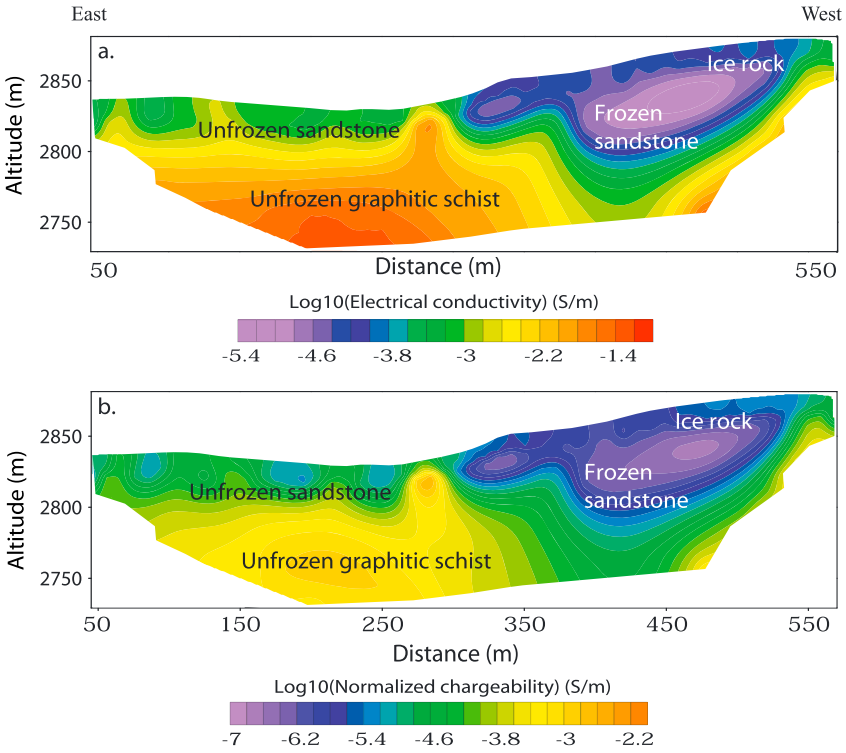

Figure 24. Large-scale electrical conductivity and normalized chargeability tomograms crossing the area of interest (Profile P2). (a) Electrical conductivity tomogram showing position and depth of the permafrost (about 50 m). (b) Normalized chargeability tomogram high normalized chargeability zones correlated with graphitic schist formation.

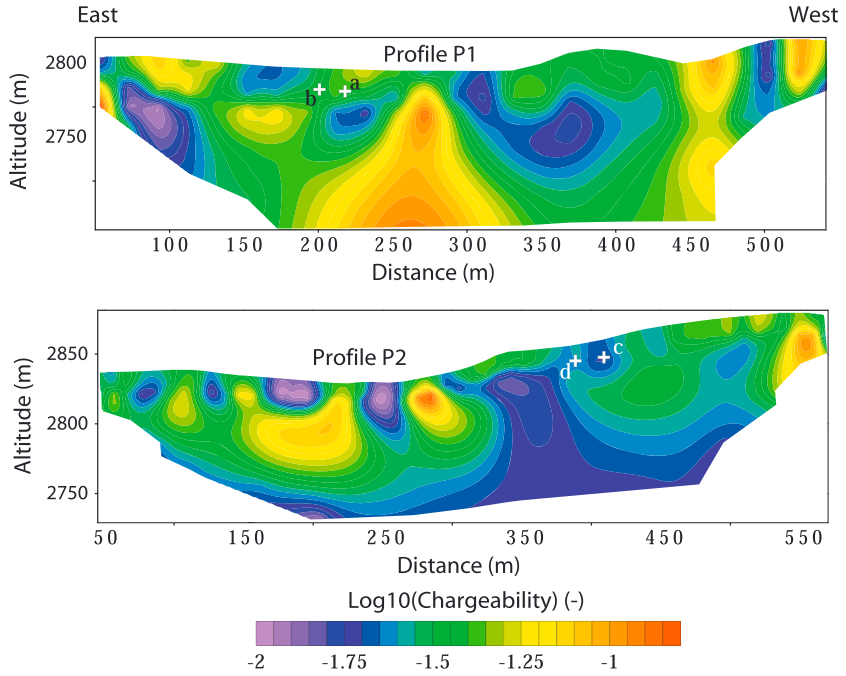

Figure 25. Large-scale electrical chargeability tomogram crossing the area of interest (Profiles 1 and 2). The high values of the chargeability (>0.1) correspond to graphite-rich zones. The labels a to d indicate the position of the quadripoles indicated in Figure 22.

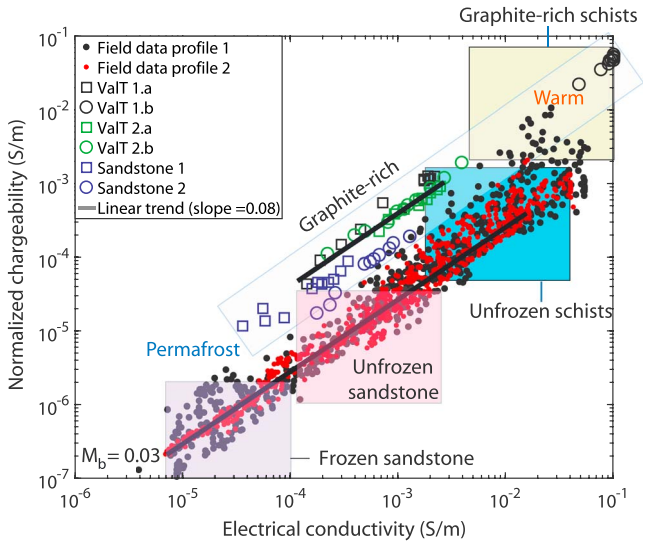

Figure 26. Normalized chargeability versus electrical conductivity at different temperatures for inverted field data (red and black filled circles) and laboratory experiments (open squares and circles). The data above the lower plain line indicate that the sample contains semiconductor or metallic particles. The normalized chargeability is calculated from the equation $M_n = M\,\sigma_\infty$, where σ_∞ and $M\,(=M1)$ come from the fitting with the double Cole-Cole model discussed in Appendix A. The grey area corresponds to the graphite-rich zone. The high and low values of the normalized chargeability and conductivity are also controlled by the lithology.

5. Conclusions

A conduction and polarization model is proposed to account for the presence of graphite in rock samples. In this model, we have assumed that graphite is below a percolation threshold. In this case, the conductivity of the material is controlled essentially by the conductivity of the background material with a small effect related to the conductivity of graphite. A strong polarization is expected with a chargeability that is linearly dependent on the volumetric amount of graphite. If graphite is above a percolation threshold, a very strong conductivity (several tens of Siemens per meter) is observed, which is concomitant with a lack of polarization of the material. This is because all the charges are free to move and therefore do not accumulate to favor polarization. Complex conductivity experiments were performed on five samples in the frequency range 10^{-2} Hz to 45 kHz and in the temperature range +20°C down to −15 °C. The data were fitted with a double Cole-Cole model and we only discussed the physical meaning of the first Cole-Cole distribution, the second one being probably a composite of the Maxwell-Wagner polarization and spurious electromagnetic effects. The Cole-Cole exponent and chargeability are essentially temperature independent as expected from the model. The relaxation time increases with the decrease of the temperature below the freezing point. At the opposite, the instantaneous conductivity decreases with the decrease of the temperature below the freezing point. The product of the two quantities is essentially temperature independent including below the freezing point. These results are consistent with the developed model and an additional numerical experiment performed with the finite element method. Further work is required to include explicitly the effect of anisotropy on the complex conductivity response of black schists. The present approach is used to image the amount of graphite in the ground.

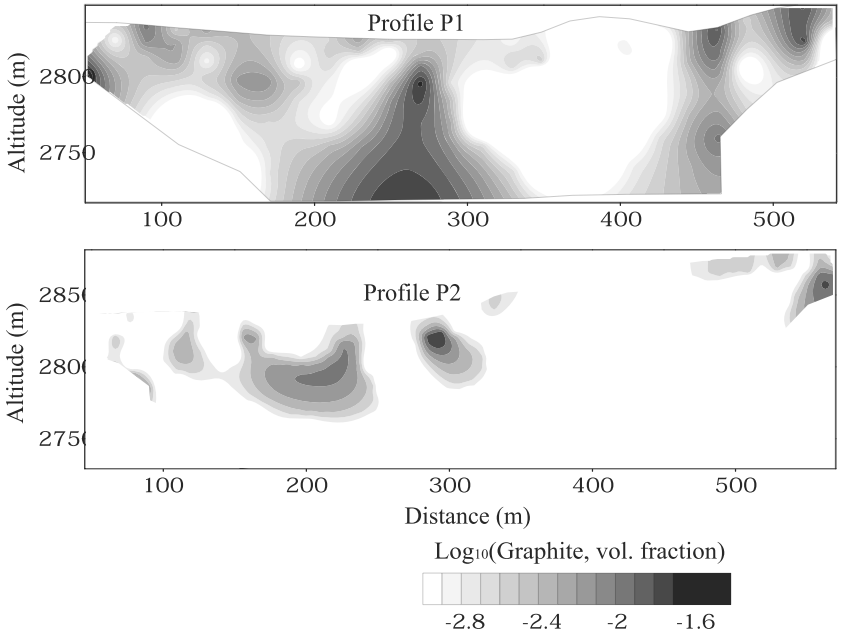

Figure 27. Estimated volume fraction of graphite along Profiles P1 and P2. The background chargeability determined from Figure 26 is $M_b = 0.03$.

Appendix A: Double Cole-Cole Parameterization and Inversion

In order to account for the induced polarization of the rock plus the Maxwell-Wagner polarization, we use a double Cole-Cole model to fit the data. Because our sample contains graphite, we will keep the index "1" to describe the first polarization and we will use the index "MW" for the Maxwell-Wagner polarization. The double Cole-Cole model is written as

$$\sigma^* = \sigma_\infty \left(1 - \frac{M_1}{1 + (i\omega\tau_1)^{c_1}} - \frac{M_{\mathrm{MW}}}{1 + (i\omega\tau_{\mathrm{MW}})^{c_{\mathrm{MW}}}}\right), \tag{A1}$$

where σ* denotes the complex conductivity, ω is the angular frequency, σ_∞ denotes the instantaneous conductivity (in S/m), M_1 and MMW denote the chargeabilities associated with the two components (nonmetallic grains and graphite), c_1 and c_{MW} are the two Cole-Cole exponents (dimensionless), and τ_1 and τMW are the (relaxation) time constants (in s). The complex conductivity spectra are inverted using this double Cole-Cole model and the nonlinear iterative method proposed by Mosegaard and Tarantola (1995) based on a Monte Carlo Markov chain sampling algorithm. The approach is described in Qi et al. (2018) and will not be repeated here.

Acknowledgments

The authors gratefully acknowledge the SETAM (Société d'Exploitation des Téléphériques Tarentaise Maurienne) for their help in this study. We thank Christophe Lambiel (UNIL) who gave the sample from Mont Fort. The numerical data and all the data used to generate the figures can be obtained by sending an e-mail to the corresponding author (A. Revil, andre.revil@univ-smb.fr). The data can also be accessed on DRYAD doi:10.5061/dryad.pt2624c. We thank X. Bodin and F. Magnin (EDYTEM) for their fruitful discussions. This study is part of the FEDER POIA *PermaRisk* project. ISTerre is part of Labex OSUG@2020 and OSUG is thanked for funding the project RESOLVE.

References

Abdulsamad, F., Florsch, N., & Camerlynck, C. (2017). Spectral induced polarization in a sandy medium containing semiconductor materials: Experimental results and numerical modelling of the polarization mechanism. *Near Surface Geophysics*, *15*, 669–683. https://doi.org/10.3997/1873-0604.2017052

Abdulsamad, F., Florsch, N., Schmutz, M., & Camerlynck, C. (2016). Assessing the high frequency behavior of non-polarizable electrodes for spectral induced polarization measurements. *Journal of Applied Geophysics*, *135*, 449–455.

Aillères, L. (1996). Structure et Cinématique de la Zone Houillère Briançonnaise entre Arc et Isère (Alpes françaises): Apport de l'inversion des Données de la Déformation Finie aux Modèles Cinématiques Classiques. Thèse INP de Lorraine, 136 pp.

Aran, D., Maul, A., & Masfaraud, J.-F. (2008). A spectrophotometric measurement of soil cation exchange capacity based on cobaltihexamine chloride absorbance. *Comptes Rendus Geoscience*, *340*(12), 865–871. https://doi.org/10.1016/j.crte.2008.07.015

Archie, G. E. (1942). The electrical resistivity log as an aid in determining some reservoir characteristics. *SPE-942054-G*. https://doi.org/10.2118/942054-G

Beyssac, O., Goffe´, B., Chopin, C., & Rouzaud, J. N. (2002). Raman spectra of carbonaceous material in metasediments: A new geothermometer. *Journal of Metamorphic Geology*, *20*, 859–871.

Börner, J. H., Girault, F., Bhattarai, M., Adhikari, L. B., Deldicque, D., Perrier, F., & Spitzer, K. (2018). Anomalous complex electrical conductivity of a graphitic black schist from the Himalayas of central Nepal. *Geophysical Research Letters*, *45*, 3984–3993. https://doi.org/10.1029/2018GL077178

Ciesielski, H., Sterckeman, T., Santerne, M., & Willery, J. P. (1997). Determination of cation exchange capacity and exchangeable cations in soils by means of cobalt hexamine trichloride. Effects of experimental conditions. *Agronomie*, *17*(1), 1–7. https://doi.org/10.1051/agro:19970101

Cole, K. S., & Cole, R. H. (1941). Dispersion and absorption in dielectrics. *Journal of Chemical Physics*, *9*, 341–351. https://doi.org/10.1063/1.1750906

Coperey, A., Revil, A., Abdulsamad, F., Stutz, B., Duvillard, P. A., & Ravanel, L. (2019). Low frequency induced polarization of porous media undergoing freezing: Preliminary observations and modeling. *Journal of Geophysical Research: Solid Earth*, *124*, 4523–4544. https://doi.org/10.1029/2018JB017015

Dahlin, T., & Leroux, V. (2012). Improvement in time-domain induced polarization data quality with multi-electrode systems by separating current and potential cables. *Near Surface Geophysics*, *10*(6), 545–656. https://doi.org/10.3997/1873-0604.2012028

Dahlin, T., Leroux, V., & Nissen, J. (2002). Measuring techniques in induced polarization imaging. *Journal of Applied Geophysics*, *50*(3), 279–298. https://doi.org/10.1016/S0926-9851(02)00148-9

Dahlin, T., & Zhou, B. (2006). Multiple-gradient array measurements for multichannel 2D resistivity imaging. *Near Surface Geophysics*, *4*(2), 113–123. https://doi.org/10.3997/1873-0604.2005037

Duvillard, P. A., Revil, A., Soueid Ahmed, A., Qi, Y., Coperey, A., & Ravanel, L. (2018). Three dimensional electrical conductivity and induced polarization tomography of a rock glacier. *Journal of Geophysical Research: Solid Earth*, *123*, 9528–9554. https://doi.org/10.1029/2018JB015965

European Commission (2017). Critical raw materials. [WWW-document] (25.1.2018).

Fabren J. (1958). Contribution à l'étude de la Zone Houillère en Maurienne et en Tarentaise (Alpes de Savoie). Thèse Université de Paris, 315 pp.

Gardent, M., Rabatel, A., Dedieu, J.-P., & Deline, P. (2014). Multitemporal glacier inventory of the French Alps from the late 1960s to the late 2000s. *Global and Planetary Change*, *120*, 24–37. https://doi.org/10.1016/j.gloplacha.2014.05.004

Ghorbani, A., Revil, A., Coperey, A., Soueid Ahmed, A., Roque, S., Heap, M. J., et al. (2018). Complex conductivity of volcanic rocks and the geophysical mapping of alteration in volcanoes. *Journal of Volcanology and Geothermal Research*, *357*, 106–127. https://doi.org/10.1016/j.jvolgeores.2018.04.014

Kirilova, M., Toy, V., Timms, N., Halfpenny, A., Menzies, C., Craw, D., et al. (2017). Textural changes of graphitic carbon by tectonic and hydrothermal processes in an active plate boundary fault zone, Alpine Fault, New Zealand. In K. Gessner, T. G. Blenkinsop, & P. Sorjonen-Ward (Eds.), *Geological Society, London, Special Publication 453, Characterization of Ore-Forming Systems From Geological, Geochemical and Geophysical Studies* (Vol. *453*, pp. 205–223). https://doi.org/10.1144/SP453.13

Landis, C. A. (1971). Graphitization of dispersed carbonaceous material in metamorphic rocks. *Contributions to Mineralogy and Petrology*, *30*, 34–45.

Loke, M. H. (2002). *RES2DINV ver. 3.50. Rapid 2-D resistivity and IP inversion using the least square method*. Penang: Geotomo Software Company.
Loke, M. H., & Barker R. (2004). RES2Dinv software. Gelugor, Malaysia: Geotomo Software Company.
Mahan, M. K., Redman, J. D., & Strangway, D. W. (1986). Complex resistivity of synthetic sulfide bearing rocks. *Geophysical Prospecting*, *34*, 743–768. https://doi.org/10.1111/j.1365-2478.1986.tb00491.x
Mao, D., & Revil, A. (2016). Induced polarization response of porous media with metallic particles.—Part 3. A new approach to time-domain induced polarization tomography. *Geophysics*, *81*(4), D345–D357. https://doi.org/10.1190/geo2015-0283.1
Marcer, M., Bodin, X., Brenning, A., Schoeneich, P., Charvet, R., & Gottardi, F. (2017). Permafrost favorability index: Spatial modelling in the French Alps using rock glaciers inventory. *Frontiers in Earth Science*, *5*. https://doi.org/10.3389/feart.2017.00105
Marshall, D. J., & Madden, T. R. (1959). Induced polarization, a study of its causes. *Geophysics*, *24*(4), 790–816.
Misra, S., Torres-Verdín, C., Revil, A., Rasmus, J., & Homan, D. (2016a). Interfacial polarization of disseminated conductive minerals in absence of redox-active species. Part 1: Mechanistic model and validation. *Geophysics*, *81*(2), E139–E157. https://doi.org/10.1190/GEO2015-0346.1
Misra, S., Torres-Verdín, C., Revil, A., Rasmus, J., & Homan, D. (2016b). Interfacial polarization of disseminated conductive minerals in absence of redox-active species. Part 2. Effective complex conductivity and dielectric permittivity. *Geophysics*, *81*(2), E159–E176. https://doi.org/10.1190/GEO2015-0400.1
Mosegaard, K., & Tarantola, A. (1995). Monte Carlo sampling of solutions to inverse problems. *Journal of Geophysical Research*, *100*(B7), 12,431–12,447. https://doi.org/10.1029/94JB03097
Olhoeft, G. (1981). Electrical properties of rocks. In Y. S. Touloukain, W. R. Judd, & R. F. Roy (Eds.), *Physical properties of rocks and mainerals* (pp. 257–330). New York: McGraw Hill.
Olhoeft, G. R. (1985). Low-frequency electrical properties. *Geophysics*, *50*, 2492–2503.
Passchier, C. W., & Trouw, R. A. J. (2005). *Micro-tectonics* (2nd ed., p. 366). Berlin Heidelberg: Springer-Verlag.
Pierson, H. O. (1993). *Handbook of carbon, graphite, diamond and fullerenes—Properties, Processing and Applications* (p. 399). New Jersey: Noyes Publications.
Qi, Y., Soueid Ahmed, A., Revil, A., Ghorbani, A., Abdulsamad, F., Florsch, N., & Bonnenfant, J. (2018). Induced polarization response of porous media with metallic particles—Part 7. Detection and quantification of buried slag heaps. *Geophysics*, *83*(5), E277–E291. https://doi.org/10.1190/GEO2017-0760.1
Revil, A. (2013). Effective conductivity and permittivity of unsaturated porous materials in the frequency range 1 mHz–1 GHz. *Water Resources Research*, *49*, 306–327. https://doi.org/10.1029/2012WR012700
Revil, A., Abdel Aal, G. Z., Atekwana, E. A., Mao, D., & Florsch, N. (2015). Induced polarization response of porous media with metallic particles—Part 2. Comparison with a broad database of experimental data. *Geophysics*, *80*(5), D539–D552. https://doi.org/10.1190/GEO2014-0578.1
Revil, A., Coperey, A., Deng, Y., Cerepi, A., & Seleznev, N. (2018). Complex conductivity of tight sandstones. *Geophysics*, *83*(2), E55–E74. https://doi.org/10.1190/GEO2017-0096.1
Revil, A., Coperey, A., Mao, D., Abdulsamad, F., Ghorbani, A., Rossi, M., & Gasquet, D. (2018). Induced polarization response of porous media with metallic particles—Part 8. Influence of temperature and salinity. *Geophysics*, *83*(6), 1–22. https://doi.org/10.1190/geo2018-0089.1
Revil, A., Coperey, A., Shao, Z., Florsch, N., Fabricius, I. L., Deng, Y., et al. (2017). Complex conductivity of soils. *Water Resources Research*, *53*, 7121–7147. https://doi.org/10.1002/2017WR020655
Revil, A., & Florsch, N. (2010). Determination of permeability from spectral induced polarization data in granular media. *Geophysical Journal International*, *181*, 1480–1498. https://doi.org/10.1111/j.1365-246X.2010.04573.x
Revil, A., Florsch, N., & Mao, D. (2015). Induced polarization response of porous media with metallic particles—Part 1: A theory for disseminated semiconductors. *Geophysics*, *80*(5), D525–D538. https://doi.org/10.1190/GEO2014-0577.1
Revil, A., Karaoulis, M., Johnson, T., & Kemna, A. (2012). Review: Some low-frequency electrical methods for subsurface characterization and monitoring in hydrogeology. *Hydrogeology Journal*, *20*(4), 617–658. https://doi.org/10.1007/s10040-011-0819-x
Schlumberger, C. (1920). *Study of underground electrical prospecting* (p. 99). Paris.
Simandl, G. J., Paradis, S., & Akam, C. (2015). Graphite deposit types, their origin, and economic significance. *British Columbia Ministry of Energy and Mines & British Columbia Geological Survey*, *3*, 163–171.
Slonczewski, J. C., & Weiss, P. R. (1958). Band structure of graphite. *Physical Review*, *109*, 272.
Vinegar, H. J., & Waxman, M. H. (1984). Induced polarization of shaly sands. *Geophysics*, *49*(8), 1267–1287.
Woodruff, W. F., Revil, A., & Torres-Verdín, C. (2014). Laboratory determination of the complex conductivity tensor of unconventional anisotropic shales. *Geophysics*, *79*(5), E183–E200. https://doi.org/10.1190/geo2013-0367.1
Wopenka, B., & Pasteris, J. D. (1993). Structural characterization of kerogens to granulite-facies graphite: Applicability of Raman microprobe spectroscopy. *American Mineralogist*, *78*, 533–557.
Zimmermann, E., Kemna, A., Berwix, J., Glaas, W., Münch, H. M., & Huisman, J. A. (2008). A high-accuracy impedance spectrometer for measuring sediments with low polarizability. *Measurement Science and Technology*, *19*(10), 105603. https://doi.org/10.1088/0957-0233/19/10/105603